Monthly Notices
of the
ROYAL ASTRONOMICAL SOCIETY

MNRAS **539,** 109–126 (2025) https://doi.org/10.1093/mnras/staf485
Advance Access publication 2025 March 25

REBELS-IFU: dust attenuation curves of 12 massive galaxies at $z \simeq 7$

R. Fisher,[1★] R. A. A. Bowler,[1] M. Stefanon,[2,3] L. E. Rowland,[4] H. S. B. Algera,[5,6,7] M. Aravena,[8] R. Bouwens,[4] P. Dayal,[9] A. Ferrara,[10] Y. Fudamoto,[11,12] C. Gulis,[13] J. A. Hodge,[4] H. Inami,[6] K. Ormerod,[14] A. Pallottini,[10] S. G. Phillips,[14] N. S. Sartorio,[15] S. Schouws,[4] R. Smit,[14] L. Sommovigo,[16] D. P. Stark[12] and P. P. van der Werf[4]

[1]*Jodrell Bank Centre for Astrophysics, University of Manchester, Oxford Road, Manchester M13 9PL, UK*
[2]*Departament d'Astronomia i Astrofísica, Universitat de València, C. Dr. Moliner 50, E-46100 Burjassot, València, Spain*
[3]*Unidad Asociada CSIC 'Grupo de Astrofísica Extragaláctica y Cosmología' (Instituto de Física de Cantabria – Universitat de València), Spain*
[4]*Leiden Observatory, Leiden University, P.O. Box 9513, NL-2300 RA Leiden, the Netherlands*
[5]*Institute of Astronomy and Astrophysics, Academia Sinica, 11F of Astronomy-Mathematics Building, No. 1, Section 4, Roosevelt Road, Taipei 106216, Taiwan, R.O.C.*
[6]*Hiroshima Astrophysical Science Center, Hiroshima University, 1-3-1 Kagamiyama, Higashi-Hiroshima, Hiroshima 739-8526, Japan*
[7]*National Astronomical Observatory of Japan, 2-21-1, Osawa, Mitaka, Tokyo, Japan*
[8]*Instituto de Estudios Astrofísicos, Facultad de Ingeniería y Ciencias, Universidad Diego Portales, Av. Ejército 441, Santiago, Chile*
[9]*Kapteyn Astronomical Institute, University of Groningen, P.O. Box 800, NL-9700 AV Groningen, the Netherlands*
[10]*Scuola Normale Superiore, Piazza dei Cavalieri 7, I-56126 Pisa, Italy*
[11]*Center for Frontier Science, Chiba University, 1-33 Yayoi-cho, Inage-ku, Chiba 263-8522, Japan*
[12]*Steward Observatory, University of Arizona, 933 N Cherry Avenue, Tucson, AZ 85721, USA*
[13]*Department of Astronomy, the Pennsylvania State University, 525 Davey Lab, University Park, PA 16802, USA*
[14]*Astrophysics Research Institute, Liverpool John Moores University, 146 Brownlow Hill, Liverpool L3 5RF, UK*
[15]*Sterrenkundig Observatorium, Krijgslaan 281 / S9, B-9000 Gent, Belgium*
[16]*Center for Computational Astrophysics, Flatiron Institute, 162 5th Avenue, New York, NY 10010, USA*

Accepted 2025 March 21. Received 2025 March 21; in original form 2024 December 21

ABSTRACT

We present measurements of the dust attenuation curves of 12 massive ($9 < \log(M_\star/\mathrm{M}_\odot) < 10$) Lyman-break galaxies at $z = 6.5$–7.7 derived from *JWST* NIRSpec integral field unit spectroscopy. The galaxies are drawn from the Atacama Large Millimeter/submillimeter Array Reionization Era Bright Emission Line Survey (REBELS) large program. The dust attenuation curves were obtained by fitting spectral energy distribution (SED) models with a flexible dust attenuation curve to the full galaxy spectra over observed wavelengths 0.6–5.3 μm. These attenuation curves show a range of recovered slopes ($-0.41 \leq \delta \leq 0.09$) that are on average slightly flatter than seen in local sources of the same stellar masses, with none exhibiting very steep slopes. Three galaxies exhibit evidence for a 2175 Å dust bump ($>4\sigma$) and we find that SED fitting excluding the bump can overestimate derived stellar masses by up to 0.4 dex. Correcting for the dust attenuation with our best-fitting attenuation curves, we recover a range of intrinsic ultraviolet slopes ($-2.4 < \beta_0 < -2.0$). The galaxies show moderate reddening ($A_{V,\,\mathrm{stellar}} = 0.1$–$0.6$ mag) and the $A_{V,\,\mathrm{stellar}}$ to stellar mass relation is consistent with local sources. The attenuation curve slope is found to correlate with $A_{V,\,\mathrm{stellar}}$, while we see no strong correlation with stellar mass, M_{UV}, or gas-phase metallicity. Overall, our results show little evolution in dust properties in the REBELS sources compared to the local Universe. Comparing our recovered trends to empirical models suggests that the most important factor driving the variation in the attenuation curves in our sample is the dust-star geometry, not the properties of the dust grains themselves.

Key words: dust, extinction – galaxies: high-redshift.

1 INTRODUCTION

In the last decade, the importance of dust in high-redshift galaxies ($z \gtrsim 4$) has been revealed through the direct detection of the redshifted greybody emission from the dust grains themselves (e.g. Watson et al. 2015; Marrone et al. 2018; Hashimoto et al. 2019; Tamura et al. 2019; Harikane et al. 2020; Bakx et al. 2021; Akins et al. 2022; Witstok et al. 2022; Algera et al. 2024a, b; Mitsuhashi et al. 2024). Atacama Large Millimeter/submillimeter Array (ALMA) programs such as the ALMA Large Program to INvestigate [C II] at Early times (ALPINE) targeting the dust content of normal star-forming galaxies at $4<z<6$ (e.g. Béthermin et al. 2020; Faisst et al. 2020; Fudamoto et al. 2020; Le Fèvre et al. 2020) and the ALMA Reionization Era Bright Emission Line Survey (REBELS) large program at $z = 6.5$–8 that targeted ultraviolet (UV)-bright galaxies

---

★ E-mail: rebecca.fisher-7@postgrad.manchester.ac.uk

($M_{\rm UV} < -21$; Bouwens et al. 2022) have revealed that nearly half of the star formation in massive ($\log(M_\star/{\rm M}_\odot) > 9$) galaxies at these redshifts is dust-obscured (e.g. Bowler et al. 2018, 2024; Fudamoto et al. 2021; Inami et al. 2022; Barrufet et al. 2023; Schouws et al. 2023; Algera et al. 2024a). However, whether the dust properties at high redshift differ significantly from those in the local Universe is still unknown.

Until recently, observations of $z \simeq 7$ galaxies have almost exclusively used photometry that probes their rest-frame UV spectral energy distributions (SEDs). The colours of galaxies can be used to infer the presence of dust since dust grains absorb and scatter the UV and optical light produced by young stars causing reddening and attenuation (e.g. Meurer, Heckman & Calzetti 1999; Draine 2003). The rest-frame UV continuum is commonly parametrized using a power-law relation, $f_\lambda \propto \lambda^\beta$ (e.g. Calzetti, Kinney & Storchi-Bergmann 1994; Meurer et al. 1999). A redder rest-frame UV slope can thus imply a larger dust content. However, β is also affected by the age, metallicity, and star formation history (SFH) of the stellar population (e.g. Bouwens et al. 2009; Castellano et al. 2014) as well as the nebular continuum (e.g. Cullen et al. 2017; Reddy et al. 2018). Due to young stellar ages at early times, dust is suggested to be the dominant factor affecting the measured β-slope (Wilkins et al. 2011; Tacchella et al. 2022). Many studies have shown that the average β value of galaxies decreases with increasing redshift, implying lower dust extinction (e.g. Bouwens et al. 2012; Dunlop et al. 2013; Topping et al. 2022b, 2024; Austin et al. 2024; Cullen et al. 2024), although some studies see no trend with redshift (e.g. Morales et al. 2024). Recent work by Roberts-Borsani et al. (2024) using NIRSpec spectra supports the trend of bluer slopes at higher redshifts. The most massive galaxies at each redshift in these samples were found to have redder slopes suggesting that these objects have a higher dust content. This is quantified by the colour–magnitude relation, β–M_{UV}, with redder UV slopes being found in the higher luminosity, more massive star-forming galaxies, suggesting that they have higher dust attenuation and/or metallicities (Reddy et al. 2010; Bouwens et al. 2014; Yamanaka & Yamada 2019; Bowler et al. 2024; Mitsuhashi et al. 2024).

At lower redshifts, the dust attenuation curve describing the wavelength-dependent effect of dust absorption and scattering of stellar photons has been inferred. The shape of this curve depends on the chemical composition of the dust, the distribution of dust grain sizes, and the dust-star spatial geometry (see Salim & Narayanan 2020 for a review). The attenuation curve can be obtained using spectroscopic observations of the Balmer emission lines and comparing the average SEDs of galaxies with different Balmer decrements (e.g. Calzetti et al. 1994; Reddy et al. 2015; Battisti, Calzetti & Chary 2016, 2017; Shivaei et al. 2020a; Battisti et al. 2022; Cooper et al. 2024). Alternatively, the attenuation curve can be obtained by comparing the SED fitted to observations to an assumed intrinsic spectrum (Cullen et al. 2018) or SED fitting with a flexible dust attenuation curve (e.g. Salim, Boquien & Lee 2018; Boquien et al. 2022; Markov et al. 2023, 2024).

Studies such as Battisti et al. (2022) suggest that the attenuation curve evolves continuously with redshift, since they find that the average dust attenuation curve slope and normalization at $z \simeq 1.3$ is between the Calzetti et al. (2000) curve from local starburst galaxies and the steeper curve of Reddy et al. (2015) at $z \simeq 2$. However, the attenuation curve slope has also been found to depend on properties other than redshift, complicating the interpretation. For example, Shivaei et al. (2020a) find that the slope of the dust attenuation curve at $z \simeq 2$ may be metallicity dependent, with lower metallicity galaxies exhibiting steeper slopes more similar to that of the Small Magellanic Cloud (SMC) extinction curve. In contrast, at $z<0.3$, Salim et al. (2018) find that the attenuation curves for individual galaxies have a wide variety of slopes with some dependence on stellar mass but no clear trend with metallicity. Additionally, more massive galaxies with older stellar populations, higher metallicities, higher star formation rates (SFRs), and higher dust attenuation magnitudes have been seen to show shallower, more Calzetti-like, dust attenuation curves (Cullen et al. 2018; McLure et al. 2018), while lower mass galaxies may have steeper, more SMC-like curves (Reddy et al. 2010, 2018; Bouwens et al. 2016; Shivaei et al. 2020a, b).

At $z \simeq 5$, Boquien et al. (2022) also find a range of attenuation curve slopes ($-1.84 \leq \delta \leq 0.23$) in a subset of the ALPINE galaxies, demonstrating that a single attenuation curve is not appropriate for these main-sequence galaxies. The shape of the attenuation curve may also deviate significantly from what is seen locally, as inferred from NIRSpec observations of H I recombination lines for a galaxy at $z = 4.41$ by Sanders et al. (2024a). These findings suggest that dust grain properties and/or dust-star geometry could differ at high redshift compared to local star-forming galaxies and can also significantly vary between galaxies. This has implications for derived properties; for example, Reddy et al. (2015) find that the assumption of the wrong attenuation curve can cause SFR and mass differences of up to 20 per cent and 0.16 dex, respectively.

With the *JWST*, we now have the spectroscopic sensitivity and wavelength coverage to measure both the shape and magnitude of dust attenuation for the first time at very high redshifts. For example, recent work by Markov et al. (2024) measuring attenuation curves at $z = 2$–12 with NIRSpec found that attenuation curve shapes may significantly deviate from those in the local universe, causing deviations in SFR and mass estimates of up to 0.4 dex compared to the typically assumed Calzetti et al. (2000) curve. This study also finds tentative evidence that the slopes flatten with increasing redshift and attributes this to larger dust grains at earlier epochs since there has been insufficient time for reprocessing in the interstellar medium (ISM) to produce smaller grains. Detailed measurements of individual galaxies have revealed evidence for the 2175 Å dust bump in the epoch of reionization (Markov et al. 2023, 2024; Witstok et al. 2023b). This bump feature is believed to be associated with small carbonaceous grains (polycyclic aromatic hydrocarbons; e.g. Draine 2003; Decleir et al. 2019; Massa, Gordon & Fitzpatrick 2022; Shivaei et al. 2022; Battisti et al. 2024; Gordon et al. 2024), implying that these grains are rapidly produced and survive in the ISM of high-redshift galaxies (see Schneider & Maiolino 2024, for a review).

In this work, we measure the dust attenuation curves directly from a sample of massive Lyman-break galaxies at $z \simeq 7$. This subset of the REBELS galaxies is a unique data set for which we have NIRSpec spectra at rest-UV and rest-optical wavelengths with a spectral resolution $R \simeq 100$. This allows us to measure the gas-phase metallicity from optical emission lines (Rowland et al. 2025) and estimate more robust stellar masses (Stefanon et al., in preparation). The galaxies at these redshifts in studies to date have lower stellar masses (e.g. Markov et al. 2023, 2024; Witstok et al. 2023b), whereas the REBELS sample probes the massive end with larger inferred dust contents and, thus, dust attenuation is expected to have a more significant effect on observed properties. The REBELS sample also uniquely benefits from far-infrared (FIR) spectral coverage from ALMA observations that can be combined with the analysis of the *JWST* observations presented here. Constraints on dust production models can also now be made using the dust-to-gas, dust-to-metal, and dust-to-stellar ratios for these galaxies (Algera et al. 2025).

Table 1. The 12 REBELS galaxies targeted with the NIRSpec IFU observations used in this study. Column (1): Galaxy identifier. Column (2): Spectroscopic redshift from the [C II] detection from ALMA (Bouwens et al. 2022). Column (3): Rest-frame UV-continuum slope, β. Column (4): Absolute rest-frame UV magnitude at 1500 Å, $M_{\rm UV}$. Column (5): Gas-phase metallicities, $Z_{\rm gas}$, derived from optical emission lines (Rowland et al. 2025). The best-fitting parameters from the BAGPIPES SED fits with a flexible dust attenuation curve are then shown. Column (6): V-band continuum attenuation, $A_{V,\,\rm stellar}$. Column (7): Slope of the dust attenuation curve expressed as the deviation, δ, of the power-law exponent from the Calzetti-like curve. Column (8): The 2175 Å dust bump strength, B. Column (9): Stellar mass, $M_\star$. Note that these differ from those presented in Stefanon et al. (in preparation) who assume a fixed Calzetti dust attenuation curve, but are consistent within the errors. Column (10): The intrinsic UV slope, β_0, of the SED model (see Section 5.5).

ID (1)	z (2)	β (3)	$M_{\rm UV}$ /mag (4)	$Z_{\rm gas}$ /Z$_\odot$ (5)	$A_{V,\,\rm stellar}$ /mag (6)	δ (7)	B (8)	$\log_{10}(M_\star/{\rm M}_\odot)$ (9)	β_0 (10)
REBELS-05	6.496	-1.42 ± 0.06	-21.49 ± 0.07	0.66 ± 0.25	$0.37^{+0.10}_{-0.09}$	$-0.18^{+0.06}_{-0.07}$	$0.18^{+0.17}_{-0.13}$	$9.60^{+0.10}_{-0.10}$	-2.13 ± 0.05
REBELS-08	6.749	-1.92 ± 0.05	-21.88 ± 0.03	0.34 ± 0.16	$0.28^{+0.08}_{-0.06}$	$-0.10^{+0.07}_{-0.08}$	$3.04^{+0.47}_{-0.44}$	$9.31^{+0.10}_{-0.10}$	-2.27 ± 0.05
REBELS-12	7.346	-1.67 ± 0.03	-22.39 ± 0.03	0.35 ± 0.11	$0.18^{+0.08}_{-0.09}$	$-0.31^{+0.20}_{-0.31}$	$0.15^{+0.21}_{-0.10}$	$9.80^{+0.09}_{-0.09}$	-2.28 ± 0.04
REBELS-14	7.084	-1.74 ± 0.03	-22.30 ± 0.04	0.16 ± 0.05	$0.17^{+0.08}_{-0.06}$	$-0.39^{+0.14}_{-0.23}$	$0.23^{+0.29}_{-0.14}$	$9.54^{+0.12}_{-0.14}$	-2.33 ± 0.05
REBELS-15	6.875	-2.01 ± 0.03	-22.40 ± 0.03	0.12 ± 0.09	$0.34^{+0.08}_{-0.06}$	$-0.03^{+0.04}_{-0.04}$	$0.98^{+0.15}_{-0.13}$	$9.40^{+0.03}_{-0.03}$	-2.30 ± 0.03
REBELS-18	7.675	-1.56 ± 0.03	-22.11 ± 0.02	0.64 ± 0.19	$0.26^{+0.04}_{-0.05}$	$-0.41^{+0.09}_{-0.10}$	$0.57^{+0.18}_{-0.16}$	$9.98^{+0.04}_{-0.04}$	-2.24 ± 0.03
REBELS-25	7.307	-1.61 ± 0.09	-21.46 ± 0.05	0.85 ± 0.33	$0.25^{+0.08}_{-0.06}$	$-0.35^{+0.13}_{-0.15}$	$2.72^{+0.61}_{-0.64}$	$9.07^{+0.10}_{-0.08}$	-2.05 ± 0.12
REBELS-29	6.685	-1.89 ± 0.05	-22.00 ± 0.04	1.11 ± 0.40	$0.33^{+0.09}_{-0.08}$	$-0.09^{+0.08}_{-0.07}$	$0.72^{+0.31}_{-0.27}$	$9.94^{+0.06}_{-0.08}$	-2.25 ± 0.06
REBELS-32	6.729	-1.34 ± 0.07	-21.16 ± 0.08	0.61 ± 0.19	$0.45^{+0.13}_{-0.12}$	$-0.09^{+0.07}_{-0.07}$	$0.55^{+0.28}_{-0.28}$	$9.75^{+0.11}_{-0.13}$	-2.19 ± 0.07
REBELS-34	6.634	-2.23 ± 0.03	-22.25 ± 0.02	0.44 ± 0.32	$0.10^{+0.05}_{-0.04}$	$-0.14^{+0.14}_{-0.17}$	$1.02^{+0.54}_{-0.53}$	$9.59^{+0.09}_{-0.08}$	-2.26 ± 0.04
REBELS-38	6.577	-1.63 ± 0.06	-21.99 ± 0.05	0.39 ± 0.17	$0.58^{+0.12}_{-0.14}$	$0.09^{+0.05}_{-0.06}$	$0.12^{+0.12}_{-0.08}$	$9.93^{+0.08}_{-0.09}$	-2.26 ± 0.06
REBELS-39	6.845	-2.07 ± 0.04	-22.39 ± 0.04	0.21 ± 0.16	$0.17^{+0.06}_{-0.04}$	$-0.23^{+0.08}_{-0.10}$	$0.95^{+0.40}_{-0.37}$	$9.57^{+0.11}_{-0.10}$	-2.29 ± 0.04

The structure of this paper is as follows. In Section 2, we introduce the REBELS integral field unit (REBELS-IFU) sample and data set. In Section 3, we describe the SED fitting set-up with a flexible dust attenuation curve and how physical properties were extracted from the galaxy spectra. In Section 4, we present the results from these fits including the dust attenuation curves for each galaxy. We discuss the implications of our results on the dust properties of these sources in Section 5. The key findings are summarized in Section 6. We assume the standard Lambda cold dark matter cosmology with $H_0 = 70$ km s^{-1} Mpc^{-1}, $\Omega_{\rm m} = 0.3$, and $\Omega_\Lambda = 0.7$ throughout this work (Planck Collaboration VI 2020).

2 DATA AND SAMPLE

The galaxies studied in this work are a subset of the 40 massive ($\log_{10}(M_*/{\rm M}_\odot) = 8.8$–$10.4$; Topping et al. 2022a)[1] Lyman-break galaxies at $z = 6.5$–9.5 targeted by the REBELS ALMA large program. This survey aimed to detect dust continuum and [C II] 158 µm emission in bright, star-forming galaxies identified from wide-field ground-based imaging and *Hubble Space Telescope* (*HST*) archival fields. A detailed summary of the selection and results from the first year of observations of the REBELS galaxies can be found in Bouwens et al. (2022).

JWST NIRSpec observations were obtained (PID 1626; P.I. Stefanon and PID 2659; P.I. Weaver, *JWST* Cycle 1) for the 12 galaxies listed in Table 1. These galaxies were selected based on having the brightest [C II] 158 µm emission in the REBELS program and SFRs inferred from [C II] of 50–400 M$_\odot$ yr^{-1} (De Looze et al. 2014). These SFRs are significantly higher than typical galaxies at these redshifts (although we note that the SFRs inferred from UV + infrared estimates tend to be slightly lower; e.g. Bowler et al. 2024). They are a representative sample of the ranges of physical properties, such as stellar mass, rest-UV slope, and [O III] + Hβ equivalent width, seen in the full REBELS sample (see Stefanon et al., in preparation).

The IFU observations consist of a spectrum between wavelengths of 0.6 and 5.3 µm for each pixel in the 3.1 arcsec × 3.2 arcsec field of view. We used the prism mode with a resolution of $R \simeq 100$ to efficiently measure both the rest-UV/optical continuum shapes and bright line emission. An exposure time of approximately 30 min per source was chosen to provide high S/N spatially resolved information in the rest-frame optical (S/N $\sim$ 8–10) and for key optical emission lines (S/N $>$ 10). To obtain a total galaxy spectrum, a source aperture for each galaxy was created by combining the 5σ isophotal contours in wavelength ranges corresponding to Hα, Hβ, UV continuum, optical continuum, [O II] $\lambda\lambda$3727, 3729, and [O III] $\lambda\lambda$4959, 5007 emission. This approach accounts for any wavelength dependence in the morphology. There was good consistency between the spectrum extracted from these pixels and previous photometry (Bouwens et al. 2022). We find that the default error extension on the cube underestimates the error by a factor of $\gtrsim$2 and, thus, we use the root mean square of the extracted spectra instead. The full details of the cube data reduction will be presented in a future paper (Stefanon et al., in preparation).

3 METHODS

We infer the best-fitting dust attenuation curves through SED fitting to the full NIRSpec PRISM spectra.The fits were performed using BAGPIPES (Carnall et al. 2018, 2019). An example fit is shown in Fig. 1 and the best-fitting parameters for each galaxy are shown in Table 1. A summary of the SED fitting parameters and the priors we used can be found in Table 2. We do not include the ALMA dust continuum measurements in these SED fits since this is non-trivial and would introduce degeneracies associated with the assumed FIR SED shape and dust geometry. Also, the dust continuum of 2 of

---

[1] Note that for the galaxies studied in this work the stellar masses are re-derived from the SED fits to the *JWST* NIRSpec spectra.

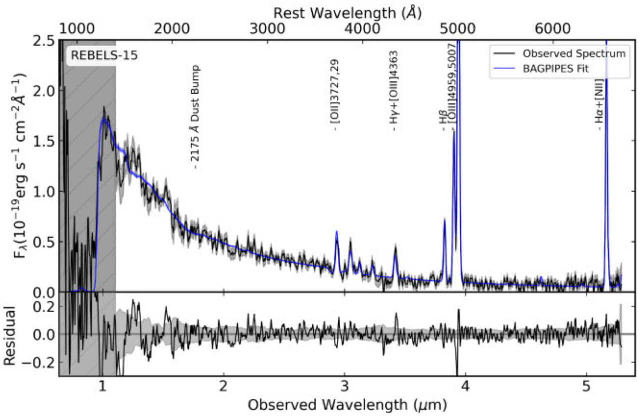

Figure 1. An example of the full NIRSpec PRISM spectrum for one of the REBELS-IFU galaxies with the 1σ error shown by the grey-shaded region. The best-fitting SED model using a flexible dust attenuation curve is shown in blue. The spectrum is masked below a rest-frame wavelength of 1400 Å (grey hatched region) to exclude effects caused by potential Ly α damping and instrumental effects at low wavelengths. The bottom panel shows the fit residuals. REBELS-15 shows evidence for a 2175 Å dust bump at ∼1.7 μm.

Table 2. The BAGPIPES SED fitting parameters and their priors used in this work. These are the redshift (z), stellar mass ($M_\star$), stellar metallicity ($Z_{\rm stellar}$), ionization parameter (U), V-band continuum attenuation ($A_{V,\,\rm stellar}$), multiplicative factor on $A_{V,\,\rm stellar}$ for the emission lines (η), the dust attenuation curve slope (δ), and the 2175 Å bump strength (B).

Parameter	Limits	Prior
z	–	Fixed
$\log_{10}(M_\star/{\rm M}_\odot)$	(7, 12)	Uniform
$Z_{\rm stellar}/{\rm Z}_\odot$	(1e−06, 10)	Logarithmic
$\log U$	(−3, 0)	Uniform
$A_{V,\,\rm stellar}$/mag	(0, 5)	Uniform
η	(1, 3)	Uniform
δ	(−2, 0.75)	Uniform
B	(0, 4)	Uniform

our sources is undetected and 8 out of the 10 detections are low S/N (∼3.5–5.3σ; Inami et al. 2022). We used a non-parametric (NP) SFH model with a continuity prior. The SFH consists of six bins. The two most recent are set to 3 and 7 Myr. The remaining four are evenly distributed in log space up to $z = 20$. NP models are more flexible and have been found to better reproduce the shape of more complex SFHs with fewer biases and smaller systematic uncertainties on the derived parameters than parametric models (Leja et al. 2019; Lower et al. 2020; Topping et al. 2022a; Markov et al. 2023; Whitler et al. 2023). Our key results are unchanged if we assume a parametric SFH (see Appendix A). We use the Bruzual & Charlot (2003) stellar population model, which uses a Kroupa (2001) initial mass function (IMF). The grids we use for the nebular line and continuum emission, generated using CLOUDY (Ferland et al. 2017), allow the log U parameter to vary in the range (−3, 0). To check whether the derived dust attenuation curves are not affected by systematics originating from our choice of stellar model, we also ran using BPASS stellar population models (Stanway & Eldridge 2018) and found that the dust attenuation curves are consistent within the errors, with no clear biases (see Appendix A).

From independent emission line fitting (Rowland et al. 2025), we find that the line dispersion of the NIRSpec spectra is lower than the pre-flight expectation by a factor of ∼1.2 (see Stefanon et al., in preparation). Therefore, we use an updated line-spread function in the fitting to account for the variable spectral resolution of the NIRSpec PRISM. The redshifts were fixed to the [C II] spectroscopic values. Small redshift offsets ($\Delta z \leq 0.01$) from the [C II] spectroscopic redshifts found during the emission line fits are accounted for by shifting the observed wavelength array of the spectra. Although direct measurements of the gas-phase metallicities using the R23/R3/O32 emission line ratios and the strong-line calibrations of Sanders et al. (2024b) have been made (see Rowland et al. 2025, for full details), we choose to leave the stellar metallicity as a free parameter with a logarithmic prior in the SED fits since the stellar metallicity is not necessarily equal to the gas-phase metallicity. This also minimizes potential systematic effects in the SED fitting arising from the limited number of templates. Additionally, we mask the spectrum at wavelengths below 1400 Å to exclude the Ly α damping region (Heintz et al. 2025) and instrumental effects at short wavelengths.

In our fits, we use the flexible dust attenuation curve model in BAGPIPES that follows the parametrization of Salim et al. (2018). This model allows flexibility in the slope of the dust attenuation curve, but can also recover the commonly used curves (e.g. Calzetti-like and SMC). The shape of the dust attenuation curve is parametrized by

$$\frac{A_\lambda}{A_{V,\,\rm stellar}} = \frac{k(\lambda,\,{\rm Calzetti})}{R_{V,\,\rm Calzetti}}\left(\frac{\lambda}{5500\,\text{Å}}\right)^{\delta} + \frac{D_\lambda(B)}{R_V}, \tag{1}$$

where $k(\lambda, \text{Calzetti})$ is the Calzetti et al. (2000) dust attenuation curve, $R_{V,\rm Calzetti} = 4.05$, δ is the deviation from the Calzetti-like attenuation curve (i.e. for a Calzetti-like curve $\delta = 0$ and for the SMC extinction curve $\delta \simeq -0.45$), A_λ is the attenuation magnitude at the wavelength λ, and $A_{V,\,\rm stellar}$ is the V-band (5500 Å) continuum attenuation magnitude (Salim et al. 2018). The second term describes the dust bump centred at $\lambda_0 = 2175$ Å that is modelled by a Drude profile

$$D_\lambda(B) = \frac{B\lambda^2 w^2}{(\lambda^2 - \lambda_0^2)^2 + \lambda^2 w^2}, \tag{2}$$

with amplitude B in units of $A_{\rm bump}/E(B-V)$ and width $w = 350$ Å. This commonly adopted width value is an intermediate value between that found for the Milky Way, Large Magellanic Cloud, and $z \simeq 2$ star-forming galaxies (e.g. Gordon et al. 2003; Fitzpatrick & Massa 2007; Noll et al. 2009) and thus we caveat that this value is not well constrained. The uncertainties on the dust attenuation curves were calculated from the errors on δ and B provided by BAGPIPES. The total-to-selective extinction ratio, R_V, is given by

$$R_V = \frac{A_{V,\,\rm stellar}}{E(B-V)_{\rm stellar}} = \frac{A_{V,\,\rm stellar}}{A_{B,\,\rm stellar} - A_{V,\,\rm stellar}}, \tag{3}$$

where A_B is the B-band (4400 Å) attenuation. Using this, we can obtain the total attenuation curve as

$$k(\lambda) = \frac{A_\lambda R_V}{A_{V,\,\rm stellar}}. \tag{4}$$

The multiplicative factor on $A_{V,\,\rm stellar}$ for stars in birth clouds, η, was also allowed to vary since measurements of nebular attenuation from the Balmer emission lines imply that this may differ from the continuum attenuation (Fisher et al., in preparation). In practice, this means that the dust attenuation applied to the emission lines in the SED fit equals η multiplied by the continuum attenuation, $A_{V,\,\rm stellar}$. Allowing this parameter to vary does not significantly change the derived shape of the dust attenuation curves; however, it does result in lower continuum $A_{V,\,\mathrm{stellar}}$ values than fits with $\eta = 1$. We caveat that our SED fitting therefore assumes that the attenuation curve affecting the nebular emission is the same as that affecting the stellar continuum, scaled by the multiplicative factor η. There is some evidence at lower redshift that the nebular dust attenuation curve is steeper than the one attenuating the stellar continuum (e.g. Calzetti 1997; Reddy et al. 2020; Rezaee et al. 2021). However, it is unknown whether this also applies at higher redshifts, with work by Sanders et al. (2024a) finding a nebular attenuation curve that significantly deviates from commonly assumed attenuation curves in a galaxy at $z = 4.41$. However, we are unable to place strong constraints on the nebular attenuation curve due to the low S/N and blending of the higher order Balmer lines in our spectra. To test the validity of our approach, we ran the SED fitting on simulated galaxy spectra and found that the dust attenuation curve is accurately recovered, with smaller errors on the dust attenuation curve slope for galaxies with higher $A_{V,\,\mathrm{stellar}}$ values, as we would expect. This is shown in Fig. A1 and discussed in Appendix A.

The rest-frame UV slope, β, was obtained directly from the observed spectra by fitting a power law between the rest-frame wavelengths $\lambda_{\mathrm{rest}} = 1268$–$2580$ Å using a least-squares fitting method. The values are consistent within the errors with those obtained if we fit using only the Calzetti windows (Calzetti et al. 1994), implying that the rest-UV region is not affected by strong emission or absorption lines in these sources. The monochromatic rest-frame UV magnitude, M_{UV}, was calculated from the spectrum flux, F_λ, in a top hat filter of width 100 Å centred at $\lambda_{\mathrm{rest}} = 1500$ Å.

4 RESULTS

4.1 Dust attenuation curves

The best-fitting dust attenuation curve for each galaxy is shown in red in Fig. 2. The curves exhibit a variety of slopes and, given the size of the shaded error regions, there are distinguishable differences between them and standard assumed curves such as the SMC extinction relation. The δ values shown in Table 1 are used to quantify the slopes of the curves with respect to the Calzetti-like curve ($\delta = 0$). REBELS-38 has a positive δ value and is the only curve shallower than the Calzetti-like curve. Four attenuation curves (REBELS-15, REBELS-29, REBELS-32, and REBELS-34) are consistent within the errors with the Calzetti-like relation. Steeper curves lying between the Calzetti-like and SMC relations are seen in three sources (REBELS-05, REBELS-08, and REBELS-39). REBELS-12 has a steeper curve but the error is such that it could be consistent with either the Calzetti-like or SMC relation. The remaining three galaxies (REBELS-14, REBELS-18, and REBELS-25) have the steepest curves, consistent within the errors with the SMC relation with $\delta \simeq -0.45$. The mean slope of the sample is $\delta = -0.19 \pm 0.15$, which is consistent with the majority of the curves lying closer to the Calzetti-like curve than the SMC, as expected for more massive, higher metallicity galaxies (e.g. Cullen et al. 2018; McLure et al. 2018; Shivaei et al. 2020a). Indeed, most are inconsistent with being as steep as the SMC curve. The three attenuation curves with the largest errors on δ are REBELS-12, REBELS-14, and REBELS-25, which all reside at $z > 7$. This means that more of the rest-optical region of the spectrum is redshifted beyond the wavelength coverage of NIRSpec. The error on REBELS-34 is also larger than the other galaxies since it has the lowest $A_{V,\,\mathrm{stellar}}$ value, meaning that dust has less of an impact on the spectrum (see Appendix A). This is unsurprising given the non-detection of the FIR dust continuum with ALMA for REBELS-34 (Inami et al. 2022).

Three galaxies (REBELS-08, REBELS-15, and REBELS-25) have bump strengths greater than zero at more than 4σ significance (7.0σ, 7.5σ, and 4.3σ, respectively). The dust attenuation curve of REBELS-08 shows evidence for a strong 2175 Å bump, with a recovered bump strength of $B = 3.04^{+0.47}_{-0.44}$. For comparison, the bump strength in the Milky Way extinction curve has a mean value of $B = 3$ (Salim et al. 2018). REBELS-25 also has a high recovered bump strength of $2.72^{+0.61}_{-0.64}$, although this attenuation curve is less well constrained, likely due to its higher redshift reducing the wavelength coverage of the rest-optical spectrum and the lower S/N of the spectrum. If we fix the bump strength to $B = 0$ in the fits for REBELS-08 and REBELS-25, we recover dust curves with shallower slopes. We compare the Bayesian information criterion ($\mathrm{BIC} = -2\ln(L) + n_{\mathrm{free}}\ln(N)$, where $\ln(L)$ is the maximum log-likelihood, n_{free} is the number of free model parameters, and N is the number of data points; e.g. Schwarz 1978; Liddle 2007) values to help assess which model is preferred. REBELS-08 and REBELS-25 are the only two galaxies for which the fits with a bump term ($n_{\mathrm{free}} = 12$) exhibit significantly lower BIC values ($\Delta\mathrm{BIC} = 65$ and 15, respectively), indicating that the model is preferred over the fits with no bump term ($n_{\mathrm{free}} = 11$). A more detailed analysis of dust bumps from the REBELS-IFU data will be presented in Ormerod et al. (in preparation).

To allow for more variety in dust attenuation curve shape, we also fit using the Li et al. (2008) parametrization that has four free parameters determining the shape of the dust attenuation curve ($n_{\mathrm{free}} = 14$). We find that the shapes agree well with the Salim model fits. The BIC values were similar in all cases with a slight preference for the Salim et al. (2018) model ($\Delta\mathrm{BIC} = 0$–16). Thus, there is no statistical evidence that the more complex model better describes the shapes of the attenuation curves, which might have implied that the shapes significantly deviate from local relations, and so we only present our results using the Salim et al. (2018) model. We caveat that the reduced wavelength coverage in the far-UV (FUV) of our spectra compared to those used in Markov et al. (2023, 2024) could be partially responsible for this. In Appendix A, we also compare to using the Charlot & Fall (2000) dust attenuation curve model ($n_{\mathrm{free}} = 11$ since this model does not include a dust bump term). For the four galaxies with the highest significance bump detections when fitting with the Salim et al. (2018) parametrization, the BIC values indicate a preference for the Salim et al. (2018) fits ($\Delta\mathrm{BIC} > 12$). For the remaining galaxies, $\Delta\mathrm{BIC} < 8$. Given the need for the dust attenuation curve model to include a dust bump, we opt to use the Salim et al. (2018) parametrization. We note that the Charlot & Fall (2000) parametrization tends to fit shallower slopes and higher $A_{V,\,\mathrm{stellar}}$ values. Despite this, our overall conclusions and trends recovered in Figs 3 and 4 are qualitatively similar if we use these different parametrizations or run the SED fitting with the emission lines in the spectra masked.

4.2 Dust attenuation curve slope dependence on physical properties

In addition to the bump feature, the dependence of the slope of the dust attenuation curve on other galaxy properties can reveal information about the composition and distribution of dust in galaxies. In Fig. 3, we plot the slope of the attenuation curve, δ, against other galaxy properties. We see a strong correlation between the

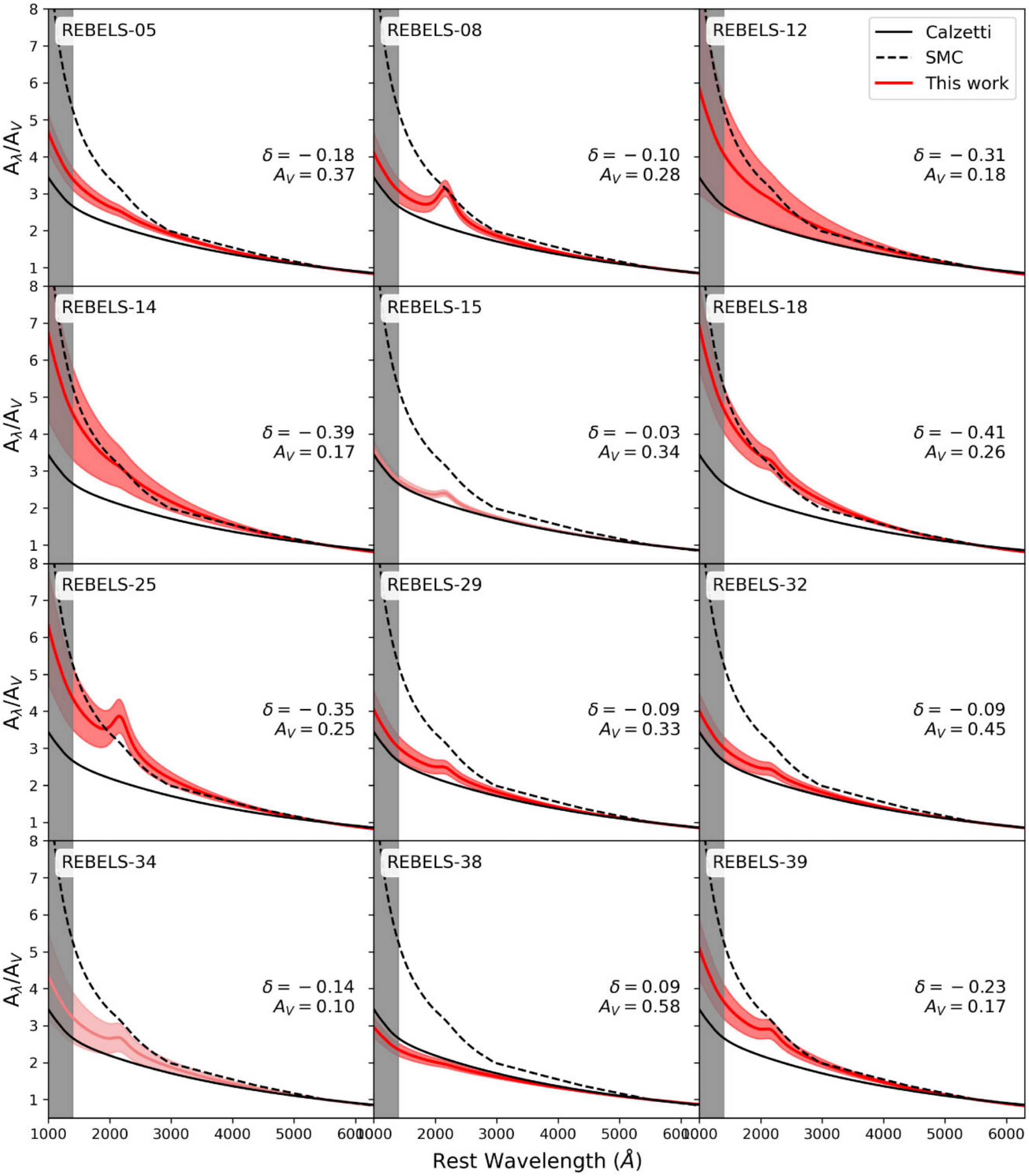

Figure 2. The best-fitting dust attenuation curves for 12 massive galaxies at $z \simeq 7$ from the REBELS-IFU program. These curves were obtained from SED fits to the global NIRSpec spectra extracted from the IFU. We use BAGPIPES to fit the SED models with an NP SFH and a Salim et al. (2018) flexible dust attenuation curve parametrization. The observed spectrum was masked below a rest wavelength of 1400 Å, as shown by the grey-shaded band. The red-shaded region shows the 1σ error on the attenuation curves. The two galaxies with no dust continuum detections (REBELS-15 and REBELS-34) are shown in a fainter shade of red. The Calzetti-like (SMC) curve is shown by the solid (dashed) black line.

dust attenuation curve slope, δ, and $A_{V,\,\rm stellar}$ (Spearman correlation coefficient $r = 0.66$, p-value $= 0.02$). No strong dependence on stellar mass, $M_{\rm UV}$, or gas-phase metallicity, Z, is seen ($|r| \leq 0.15$, p-values ≥ 0.65). We describe our results in comparison to previous studies in detail below.

4.2.1 Comparison to other studies

In the top left plot of Fig. 3, we plot δ against stellar mass and find no significant correlation. This is consistent with the results for a subsample of the ALPINE galaxies at $z = 4.4$–5.5 from Boquien

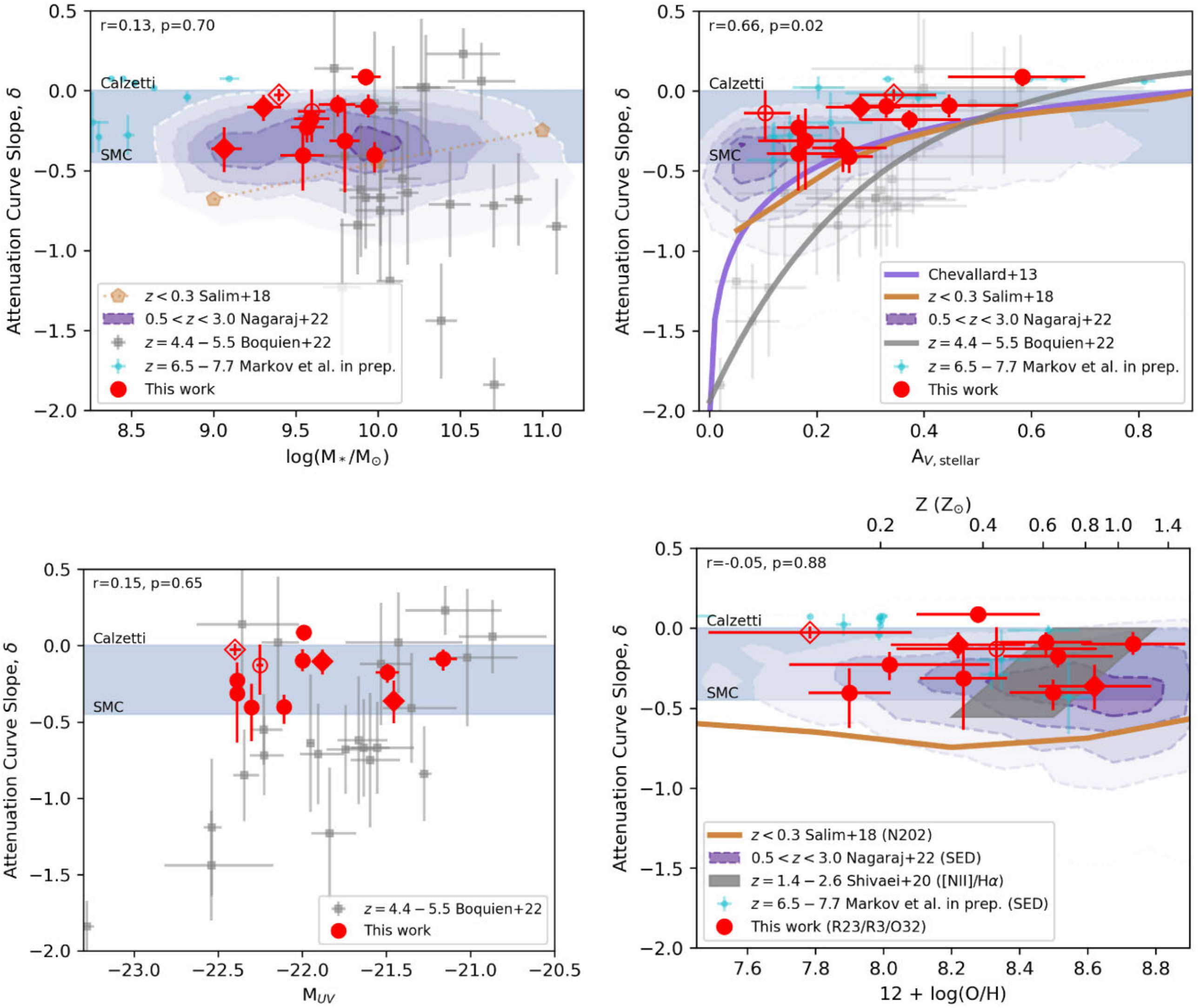

Figure 3. The derived dust attenuation curve slopes of the 12 massive galaxies from the REBELS-IFU sample at $z \simeq 7$ plotted against physical properties. The slope is expressed as the deviation, δ, of the power-law exponent from the Calzetti-like curve. The slope correlates with $A_{V,\,\mathrm{stellar}}$ (top right), but we find no clear correlations with stellar mass ($M_\star$), M_{UV}, or the gas-phase metallicities derived by Rowland et al. (2025). The Calzetti-like (SMC) values of $\delta = 0$ ($\delta = -0.45$) lie at either edge of the shaded grey-blue region. The average attenuation curve slopes from Shivaei et al. (2020a) for low- and high-metallicity (Z) galaxies at $z = 1.4$–2.6 are shown by the grey-shaded region in the bottom right panel. The method used in each study to obtain the metallicity measurements is indicated in parentheses in the legend. The median trend for galaxies at $z<0.3$ from Salim et al. (2018) is shown in brown and results for the $z \simeq 5$ ALPINE galaxies from Boquien et al. (2022) by grey squares. The subsample of the galaxies studied in Markov et al. (2024) and Markov et al. (in preparation) lying in the same redshift range as the REBELS-IFU sample are shown by the blue points and the purple contours show the results for the 3D-HST galaxies at $0.5<z<3.0$ from Nagaraj et al. (2022). The δ–$A_{V,\,\mathrm{stellar}}$ relation from radiative transfer modelling by Chevallard et al. (2013) is shown by the purple line. Galaxies with significant ($\gtrsim 4\sigma$) dust bumps have diamond markers and open markers are used for galaxies without an ALMA dust continuum detection.

et al. (2022) (which exhibit a greater scatter in δ values) and for the subsample of the galaxies from Markov et al. (2024) (and Markov et al., in preparation) that reside at the same redshifts as the REBELS-IFU sample, $z = 6.5$–7.7. We also compare to the results of Nagaraj et al. (2022), who use a 5D linear interpolation model to control the dust attenuation curves for the SED fits of the 3D-HST galaxies at $0.5<z<3.0$, which also show no trend with stellar mass. Nagaraj et al. (2022) find that the dependence of the attenuation curve slope on mass is complex. Local studies such as Battisti et al. (2017), which looked at 5500 $z<0.1$ star-forming galaxies, also find no trend. This is in contrast to the trend seen in local star-forming galaxies at $z<0.3$ by Salim et al. (2018) who find flatter curves at higher masses. Results from the VANDELS galaxies at redshift $z = 3$–4 by Cullen et al. (2018) have also presented tentative evidence for steepening of the attenuation curve at $\log_{10}(M_\star/\mathrm{M}_\odot) \lesssim 9.0$.

In the top right panel, we plot δ against $A_{V,\,\mathrm{stellar}}$ and find that the slopes of our galaxies get flatter with increasing $A_{V,\,\mathrm{stellar}}$. On average, the REBELS-IFU attenuation curve slopes are flatter than seen in local galaxies and the points are slightly offset from some of the lower redshift trends shown, such as the median relation from Salim et al. (2018) and the results from Boquien et al. (2022). The 23 galaxies from Boquien et al. (2022) reach low $A_{V,\,\mathrm{stellar}}$ values even though the selection required them to have an ALMA dust continuum or [C II] 158 μm detection, which means that for a given stellar mass, the sample is biased towards the more dust-rich galaxies within the ALPINE sample. Similar trends to these are also seen for

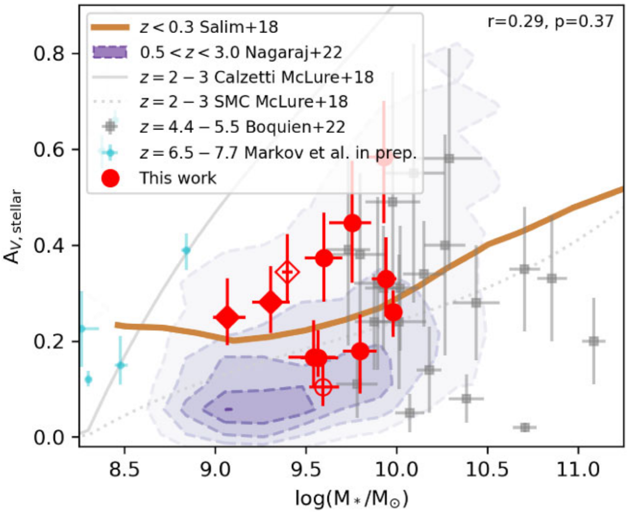

Figure 4. V-band continuum attenuation, $A_{V,\,\mathrm{stellar}}$, versus stellar mass, $M_\star$, values for the REBELS-IFU sample are shown in red. Galaxies with significant ($\gtrsim 4\sigma$) dust bumps have diamond markers and open markers are used for galaxies without an ALMA dust continuum detection. We see a weak positive correlation consistent with trends seen in local galaxies. For example, the median trend for galaxies at $z<0.3$ is shown in brown (Salim et al. 2018) and the results for the 3D-HST galaxies at $0.5<z<3.0$ are shown with purple contours (Nagaraj et al. 2022). The empirical relations for $2<z<3$ galaxies derived by McLure et al. (2018) assuming a Calzetti (SMC) attenuation curve are shown by the solid (dashed) grey lines. Results for a subsample of the ALPINE galaxies at $z = 4.4$–5.5 from Boquien et al. (2022) are shown by grey squares and the subsample of the galaxies studied in Markov et al. (in preparation) lying at the same redshift range as the REBELS-IFU sample are shown by blue circles.

the COSMOS galaxies at $0.1<z\lesssim 3$ by Battisti et al. (2020). We also compare to the results from the 3D-HST galaxies (Nagaraj et al. 2022), which show a flatter trend between δ and $A_{V,\,\mathrm{stellar}}$ that is more consistent with the position of the REBELS-IFU galaxies and the $z\simeq 7$ galaxies in the Markov et al. (in preparation) sample. Nagaraj et al. (2022) attribute the flattening of the relation they see compared to other literature results to be due to the UV spectrum being dominated by stars that have older ages and redder colours on average and/or that are surrounded by a reduced amount of birth cloud dust in their modelling. The Nagaraj et al. (2022) sample is also mass-complete and is therefore arguably the least biased of the studies shown. We also note that there are important differences in the SED fitting between the studies we compare to. In particular, Salim et al. (2016), Battisti et al. (2017, 2020), and Boquien et al. (2022) use constraints from the FIR emission whereas, as in this work, Cullen et al. (2018), Nagaraj et al. (2022), and Markov et al. (2024) do not use any FIR constraints. It has been shown that including constraints from the dust emission can help to break the degeneracy between age and dust (see Salim & Narayanan 2020, and references therein). For example, Lower et al. (2022) find that including an FIR constraint reduces the scatter in the recovered attenuation curves, although the median recovered curves are not significantly different. However, Lower et al. (2022) assume the use of broad-band photometry in the rest-UV/optical. These different methods could lead to different biases in the recovered attenuation curves; however, there are clear advantages to using our NIRSpec spectra to recover the attenuation curve slopes and bump strengths compared to broad-band studies.

The strong correlation between the slope of the dust attenuation curve and $A_{V,\,\mathrm{stellar}}$ seen in observations can be reproduced using radiative transfer models. The trend is thought to be consistent with larger effective dust optical depths and radiative transfer effects that cause the dust attenuation curve to become shallower. The relationship between dust attenuation optical depth and attenuation curve slope has been derived by both analytical modelling (Bruzual, Magris & Calvet 1988) and numerically by radiative transfer codes (e.g. Witt, Thronson & Capuano 1992; Witt & Gordon 2000; Gordon et al. 2001; Chevallard et al. 2013). For example, the models of Seon & Draine (2016) and Inoue et al. (2006), which include a clumpy ISM structure, predict that the steepest curves occur when the column density of dust is lowest. Inoue (2005) also finds that the amount of dust in young star-forming regions compared to the diffuse ISM (differential reddening) also plays a key role in determining the slope of the attenuation curve. We find that $A_{V,\,\mathrm{stellar}}$ and δ correlate with the 100 Myr SFR and it has been suggested that optical depth tends to increase with SFR. This can be explained by the more massive stars on average facing more dust attenuation at higher SFRs since the birth clouds have an increased dust enrichment compared to the diffuse ISM (Nagaraj et al. 2022). Furthermore, more recent work has shown that variations in the observed attenuation curves are seen even in simulations of individual molecular clouds depending on the line of sight or age (Di Mascia et al. 2024).

The fact that our δ values and the $z\simeq 7$ galaxies from Markov et al. (in preparation) are consistently shifted towards shallower slopes compared to the lower redshift trends is in line with the redshift evolution of the dust attenuation curve slope found in Markov et al. (2024). However, our slopes are still generally steeper than the average curve at these redshifts from Markov et al. (2024). We find no evidence for very steep slopes ($\delta < -0.5$) as found in Boquien et al. (2022), although these preferentially occur at $A_{V,\,\mathrm{stellar}}\lesssim 0.1$, where we only have one source.

We find that the attenuation curve slope shows no clear trend with M_{UV}, although the REBELS galaxies are biased towards being UV-bright. This is consistent with the lack of correlation between δ and stellar mass since we expect brighter galaxies to be more massive according to the $M_{\mathrm{UV}}-M_\star$ relation (e.g. Duncan et al. 2014).

In the bottom right panel, we use the gas-phase metallicities derived from the optical emission line ratios using the same NIRSpec spectra (Rowland et al. 2025). The REBELS-IFU sample covers a range of gas-phase metallicities, but no significant trend is seen. The lack of significant correlation of δ with metallicity is consistent with the results of Salim et al. (2018) and Battisti et al. (2017). We note that the majority of the Salim et al. (2018) sample lies in a narrow metallicity range between $12+\log(\mathrm{O/H}) = 8.5$ and $12+\log(\mathrm{O/H}) = 9.5$ and thus the metallicity range we show is not well sampled by these galaxies. The 3D-HST galaxies from Nagaraj et al. (2022) and the galaxies from Markov et al. (in preparation), which mainly reside at the higher and lower metallicity end of our sample, respectively, also show no clear trends. This is in contrast to results at $z = 1.4$–2.6 from Shivaei et al. (2020a) that found the average attenuation curve for higher metallicity galaxies ($12+\log(\mathrm{O/H}) > 8.5$) to be more Calzetti-like with evidence of a bump, while for lower metallicity galaxies ($8.2<12+\log(\mathrm{O/H})<8.5$) the curve was found to be steeper and exhibit no significant bump. This would imply that dust grains have different properties, with younger, lower metallicity environments containing smaller grains formed from the reprocessing of larger grains by ionizing radiation. The fact that a trend is seen in Shivaei et al. (2020a) but not in other work could be a result of selection biases, the narrower metallicity range probed, or the fact that the grouping of the galaxies by metallicity effectively groups the galaxies by stellar mass while other studies consider each galaxy individually. Interestingly, the galaxy in our sample with the lowest gas-phase metallicity, REBELS-15, has a slope consistent with the Calzetti-like value and a significant (7.5σ) bump detection. This is the opposite trend to Shivaei et al. (2020a). The fact that we and the majority of other studies see no trend could be consistent with the theory that geometry and orientation effects play more of a role in the attenuation curve shape than the optical properties of the dust grains themselves in high-redshift galaxies (Chevallard et al. 2013; Sommovigo et al. 2025).

4.3 $A_{V,\,\mathrm{stellar}}$–$M_\star$ relation

The total effect of dust on the observed galaxy spectra depends on the shape of the attenuation curve and the total dust attenuation, which is quantified by the value of $A_{V,\,\mathrm{stellar}}$. Plotted in Fig. 4 are the $A_{V,\,\mathrm{stellar}}$ values we derive as a function of stellar mass. The $A_{V,\,\mathrm{stellar}}$ values range between 0.10 and 0.58, indicating that there is significant attenuation by dust in these sources, and there is a weak positive correlation with stellar mass ($r = 0.29$, p-value $= 0.37$). The recovered $A_{V,\,\mathrm{stellar}}$ values are consistent with previous SED fitting to rest-UV photometry (Inami et al. 2022) and also show a positive correlation with the dust masses derived from [C II] in Sommovigo et al. (2022) that range between $\log(M_{\mathrm{dust}}/\mathrm{M}_\odot) = 6.95$ and $\log(M_{\mathrm{dust}}/\mathrm{M}_\odot) = 7.55$.

The REBELS-IFU sample fills in the parameter space between the mainly lower mass galaxies from Markov et al. (in preparation) and the 23 higher mass galaxies selected by Boquien et al. (2022) from the ALPINE survey at $z = 4.4$–5.5. The $A_{V,\,\mathrm{stellar}}$ values from these two studies were also derived from SED fitting with a flexible dust attenuation curve. Many of the REBELS-IFU galaxies lie close to the median trend derived from SED fitting with a flexible dust attenuation curve for local galaxies at $z<0.3$ by Salim et al. (2018). The positions of the REBELS-IFU galaxies also agree well with the area of the plot occupied by the 3D-HST galaxies from Nagaraj et al. (2022). The shape of the $A_{V,\,\mathrm{stellar}}$–$M_\star$ relation can be used to infer the slope of the dust attenuation curve with certain assumptions. The majority of our galaxies sit between the two grey curves derived from the UV-continuum slopes of 8407 galaxies as a function of stellar mass at $2<z<3$ spanning a mass range of $8.5 < \log(M_\star/\mathrm{M}_\odot) < 11.5$ by McLure et al. (2018) assuming a Calzetti (solid line) or SMC (dashed line) and intrinsic UV slope of $\beta_0 = -2.3$, roughly consistent with their attenuation curve slopes. The consistency of the positions of the points with the trends from other work suggests that the relation between these parameters in star-forming galaxies does not significantly evolve with redshift.

5 DISCUSSION

We have derived the dust attenuation curves from *JWST* NIRSpec spectra of 12 Lyman-break galaxies at $z = 6.5$–7.7. This is the first time dust attenuation curves have been measured from the rest-UV to optical spectra for these massive galaxies at $z \simeq 7$. We will discuss the features of these curves and the implications of the dependence of the dust attenuation curve slope on physical properties in Sections 5.1 and 5.2. In Section 5.3, we briefly discuss our results in the context of previous work using ALMA observations of these sources. We investigate the impact of fitting using flexible dust attenuation curves on other physical parameters derived from SED fits compared to assuming a fixed Calzetti-like dust attenuation curve in Section 5.4 and measure the intrinsic UV slopes of the galaxies in Section 5.5.

5.1 Dust attenuation curves in massive $z \simeq 7$ galaxies

The positions of the $A_{V,\,\mathrm{stellar}}$–$M_\star$ points for the REBELS-IFU galaxies in Fig. 4 are indicative of moderate reddening and are roughly consistent with the relation seen in local galaxies, with more massive galaxies having greater dust attenuations. Similarly, we find that δ correlates with $A_{V,\,\mathrm{stellar}}$ but not with gas-phase metallicity (Fig. 3), which is also consistent with trends in local galaxies. This suggests that evolved galaxies at $z \simeq 7$ have similar dust attenuation properties to galaxies in the local Universe. Further support for this conclusion comes from studies in the FIR that find no clear evolution with redshift of the dust emissivity index, β_{IR} (e.g. da Cunha et al. 2021; Bendo et al. 2023; Witstok et al. 2023a; Algera et al. 2024b; Tripodi et al. 2024).

Our dust attenuation curves are generally flatter than local sources with similar stellar masses, with no evidence for very steep slopes ($\delta < -0.5$) or significant shape deviations from local relations. In all but one case, the dust attenuation curves shown in Fig. 2 lie between the Calzetti-like and SMC relations. The majority are more consistent with the Calzetti-like relation than the steeper SMC curve. This is consistent with previous indirect constraints placed on the dust attenuation curves of the REBELS galaxies using ALMA observations of the FIR SED and the infrared-excess (IRX)–β relation (Schouws et al. 2023; Bowler et al. 2024). This is also consistent with other results for galaxies with high stellar masses ($\log(M_\star/\mathrm{M}_\odot) > 9$; e.g. Cullen et al. 2018; McLure et al. 2018). Other studies using NIRSpec spectra at high redshift such as Markov et al. (2024) present tentative evidence that attenuation curves get flatter with increasing redshift from $z \simeq 2$ to $z \simeq 12$. This is interpreted as being due to larger dust grains at earlier times. However, the REBELS attenuation curves we derive are generally steeper than the median curve for the corresponding redshift range in this study. This could suggest that the evolution of the attenuation curve slope is not as strong as Markov et al. (2024) suggest due to their bias towards slightly lower mass galaxies. This is supported by Nagaraj et al. (2022), who find that the redshift evolution of the dust attenuation curve is strongest for galaxies with lower masses and SFRs.

Three of our galaxies (25 per cent) exhibit $\gtrsim 4\sigma$ evidence for a 2175 Å dust bump. This suggests that small carbonaceous dust grains could be present in a significant fraction of epoch of reionization galaxies. We note that the bump strengths in our attenuation curves provide lower limits on the bump strengths in the *extinction* curves of these galaxies (Salim & Narayanan 2020). Evidence for dust bumps has been found in the spectra of several epoch of reionization galaxies (Markov et al. 2023, 2024; Witstok et al. 2023b). This is surprising given that bumps are thought to be less common at early epochs due to the time needed for carbonaceous grains to build up. Witstok et al. (2023b) find evidence for dust bumps in 10 out of 49 ($\simeq$20 per cent) sources over $z = 4.02$–7.20, with the galaxies exhibiting bumps having considerable dust attenuation (the stack of these sources had a nebular extinction derived from the Balmer decrement of $E(B - V) = 0.33 \pm 0.01$ mag) and slightly elevated metallicities compared to the rest of the sample. Our sample is too small to robustly determine whether there is a slightly elevated prevalence of the bump due to our galaxies probing the massive, dust-rich end of the population at these redshifts. Other studies suggest that bump strengths are correlated with metallicity, age, and stellar mass (e.g. Noll et al. 2009; Shivaei et al. 2020a, 2022) as well as the steepness of the dust attenuation curve (e.g. Kriek & Conroy 2013; Seon & Draine 2016; Narayanan et al. 2018). However, we see no clear trends within our sample.

5.2 The impact of geometry on attenuation curve slope

The steepness of the dust attenuation curve can be affected by the properties of the dust itself such as the grain size distribution (e.g. Hirashita & Murga 2020; Langeroodi et al. 2024), the dust distribution relative to the stars in the ISM, and higher concentrations of dust in star-forming regions (differential reddening). Radiative transfer models predict a broad range of attenuation curve shapes based on the variation of these properties (e.g. Seon & Draine 2016). The steepening of a dust attenuation curve can be explained physically by the fact that red light is scattered more isotropically at low optical depths compared to blue light, which experiences more forward scattering and therefore more absorption (Leja et al. 2017). Shallower curves are produced at high optical depths since more of the observed light originates from outside the equatorial plane of the galaxy and is therefore less affected by the wavelength-dependent scattering differences (Nagaraj et al. 2022).

The relative geometric distribution of dust and stars strongly affects the attenuation curve shape (Salim & Narayanan 2020). In particular, the studies of Di Mascia et al. (2024) and Sommovigo et al. (2025) show that a changing line of sight can strongly change the perceived attenuation in the UV and FUV regimes due to geometric effects. This is indirectly supported by Cochrane et al. (2024), who showed that orientation effects may be responsible for some '*HST*-dark' galaxies. The correlation of the slope of the dust attenuation curves with $A_{V,\,\mathrm{stellar}}$ but not with stellar mass, M_{UV}, or gas-phase metallicity seen in Fig. 3 suggests that geometry is the dominant factor affecting the attenuation curves in our sample. The more irregular rest-UV/optical morphologies seen at higher redshifts suggest that the role of geometry may become even more dominant at these redshifts (e.g. Huertas-Company et al. 2016, 2024; Faisst et al. 2017). From the improved spatial resolution of the IFU compared to ground-based VISTA imaging of the REBELS galaxies, it is evident that these massive galaxies have complex geometries and are often formed of multiple clumps (see fig. 1 of Bowler et al. 2022; Rowland et al. 2025). This was predicted by numerical simulations (Kohandel et al. 2020; Pallottini et al. 2022) and it is also seen in other bright galaxies at $z \simeq 7$ and at lower redshifts (e.g. Guo et al. 2015; Barisic et al. 2017; Bowler et al. 2017; Lines et al. 2024). Indeed, modelling by Witt & Gordon (2000) found that the trend of an increasingly grey attenuation curve with increasing dust column density was stronger in models with clumpy dust embedded in the galaxy.

The variations we see in the slopes of the attenuation curves are likely the result of a combination of effects. For example, unobscured stellar populations may flatten the curves, while scattering and different optical depths towards stellar populations of different ages may steepen the curve (Lin et al. 2021). Modelling by Boquien et al. (2022) showed that flatter attenuation curves are obtained at fixed $A_{V,\,\mathrm{stellar}}$ if the stellar distribution is more extended than the dust. This is explained physically by a higher fraction of stars being located at the edge of the clouds where they experience lower optical depths, particularly at shorter wavelengths. This could be a contributing factor for REBELS-25 where we see rest-UV clumps extending beyond the ALMA dust detection (Rowland et al. 2024), probably due to differential dust obscuration since high spatial resolution dust continuum detections exhibit very different morphologies to the rest-UV. Boquien et al. (2022) also find that geometry plays a more important role than the exact model they use for their dust grain extinction curve.

Although we have been able to constrain the shape of the dust attenuation curves, the information this reveals about dust production mechanisms is limited. Models, such as those of Seon & Draine (2016), have shown that the shape of attenuation curves is primarily determined by the wavelength dependence of the absorption, not the underlying extinction curve, meaning that the derived attenuation curve of the galaxy cannot uniquely constrain the extinction curve. In agreement with this, models by Lin et al. (2021) have shown that a wide range of extinction curves can produce similar attenuation curves. However, this modelling also shows that additional constraints may be possible in the future using ALMA observations of the FIR SED and the IRX–β relation. This highlights the value of the multiwavelength observations available for the REBELS galaxies.

5.3 Comparison to FIR observations

While a full comparison to FIR properties is beyond the scope of this paper, we discuss briefly here the ALMA properties of the sources. When we compare to previous work based on the ALMA observations of these galaxies, we see sensible trends such as blue ($\beta < -2$) UV slopes in the two galaxies (REBELS-15 and REBELS-34), which show no dust continuum detections from ALMA (Inami et al. 2022). REBELS-34 also has the lowest $A_{V,\,\mathrm{stellar}}$ value. Consistent with what we would expect from local relations (Section 4.2), larger $A_{V,\,\mathrm{stellar}}$ and δ values are seen in galaxies with higher FIR to UV luminosity ratios (IRX; Algera et al. 2024b; Bowler et al. 2024). Similarly, the dust masses derived from [C II] presented in Sommovigo et al. (2022) (and Algera et al. 2024b, for REBELS-25) correlate positively with both $A_{V,\,\mathrm{stellar}}$ and δ, except for REBELS-25, which is an outlier. This implies that including the ALMA data in the SED fitting may be important for sources with high FIR luminosities and large obscured star formation fractions such as REBELS-25. Since the dust is spatially offset from the rest-UV emission in REBELS-25 (Rowland et al. 2024) its observed spectrum could be dominated by the UV-luminous regions with lower dust obscuration, causing $A_{V,\,\mathrm{stellar}}$ to be underestimated. Spatially resolved SED fitting is needed to investigate this further.

Comparison with quantities derived from the rest-frame FIR observations also supports the physical interpretation of our results. If the flattening of attenuation curves seen in our sample is due to radiative transfer effects in a clumpy medium, we should see flatter slopes in galaxies with a higher molecular index,[2] $I_{\mathrm{m}} = (F_{158}/F_{1500})/(\beta - \beta_0)$, where F_{158} is the observed FIR continuum flux at $\lambda_{\mathrm{rest}} \approx 158$ µm and F_{1500} is the observed UV-continuum flux at $\lambda_{\mathrm{rest}} = 1500$ Å (see Ferrara et al. 2022; Inami et al. 2022, for details). Generally, the galaxies with shallower dust attenuation curves have higher molecular indices, which supports our geometrical interpretation. For example, REBELS-38 has the flattest slope and the highest $I_{\mathrm{m}} = 1787$. However, the exception to this trend is REBELS-25, which has a similar $I_{\mathrm{m}} = 1772$ value suggesting that it is equally clumpy but it exhibits a steeper attenuation curve slope. This could suggest that, while geometry seems to dominate in the majority of our sample, other factors such as the changing size distribution of grains may also be important in some sources since the shape of the attenuation curve depends on a complex combination of effects. However, we caveat again that the spectrum of REBELS-25 may be dominated by regions of lower dust obscuration.

Finally, we also find that $A_{V,\,\mathrm{stellar}}$ and δ positively correlate with the spatial offsets between the UV and dust continuum calculated by

---

[2] Large molecular indices are only possible if the UV and FIR emitting regions are spatially decoupled, with the FIR continuum emission originating from optically thick star-forming clumps that are likely to be giant molecular complexes.

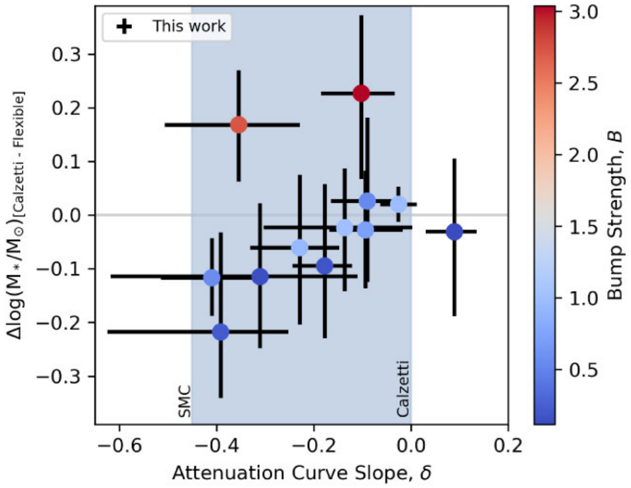

Figure 5. Stellar mass difference between SED fits assuming a Calzetti-like dust attenuation curve and with a flexible dust attenuation curve, shown against the best-fitting dust attenuation curve slope. The points are coloured by the strength of the 2175 Å dust bump. The difference in stellar mass correlates with the deviation of the dust attenuation curve slope from the Calzetti-like relation except for galaxies with a strong dust bump. In these two cases, the assumption of a Calzetti-like attenuation curve results in their masses being overestimated by up to 0.3 dex.

finding the offset between the peaks of the 2D Gaussian fits to the rest-UV and dust continuum images in Inami et al. (2022). Again, this supports that geometric effects play an important role in our attenuation curves since these UV-dust offsets imply that different star-forming regions have different dust obscurations. Future work utilizing recently obtained high spatial resolution ALMA dust continuum observations is needed to understand the dust properties of these sources in greater detail and will be the subject of a future paper (Fisher et al., in preparation). Better constraints on systematics such as dust temperatures from ongoing observations will also improve combined *JWST*-ALMA analysis.

5.4 Impact of assuming dust attenuation curves on galaxy properties

Since assuming a standard dust attenuation curve template is common in SED fitting, we investigated the impact assuming a Calzetti-like dust attenuation curve has on the derived galaxy properties. In Fig. 5, we show the differences in the stellar mass values derived with a flexible dust attenuation curve compared to SED fitting with a fixed Calzetti-like dust attenuation curve. Unsurprisingly, the stellar mass differences are negligible, with a median of 0.07 dex, owing to the similarity in the slope of the dust attenuation curves to Calzetti and correlate with δ if no strong dust bump is present. Assuming a Calzetti-like dust attenuation curve produces masses up to 0.23 dex larger in the two galaxies with the strongest dust bumps (REBELS-08 and REBELS-25). The true masses are lower since the bump feature results in a rest-UV flux deficit. If instead we fix the dust attenuation curve to the SMC relation, the mass differences are slightly larger, up to a maximum of 0.41 dex for REBELS-08. We note that any differences in the masses used in this work to those derived from SED fits assuming a Calzetti-like dust attenuation that are presented in Stefanon et al. (in preparation), Algera et al. (2025), and Rowland et al. (2025) are not significant enough to affect the trends discussed in these studies.

The size of the mass differences are consistent with previous results for the REBELS galaxies from SED fits to photometry by Topping et al. (2022a) that found masses from the fits assuming an SMC dust curve were on average 0.09 dex lower than those assuming a Calzetti attenuation curve. Topping et al. (2022a) also shows that the differences from the assumed SFH are more significant than from the assumed dust attenuation curve. These results are also consistent with other studies that compare derived properties found using a Calzetti-like curve to a flexible attenuation curve. For example, at $z \simeq 5$ Boquien et al. (2022) find that the fractional change in their mass estimates is 0.08 ± 0.14 and in local (z<0.3) galaxies Salim et al. (2016) found that assuming a Calzetti dust attenuation curve produced masses that were on average only 0.06 dex lower than with a modified attenuation curve.

Our $A_{V,\,\mathrm{stellar}}$ values can deviate by up to 0.39 dex and the SFR averaged over 100 Myr by up to 0.18 dex when using a Calzetti-like curve compared to using the derived attenuation curves. As expected, the change is less than that found in Topping et al. (2022a), who find that SFRs could differ by up to 0.4 dex when comparing results using Calzetti to SMC because the spectra provide more information than photometry. Markov et al. (2023) found that stellar masses, SFRs, and $A_{V,\,\mathrm{stellar}}$ values stay consistent within 1–2σ when assuming a Calzetti-like curve compared to the flexible model in three galaxies at $z = 7$–8. The larger deviations of up to 0.4 dex when assuming an SMC or Milky Way dust in this study are only seen in the galaxies with very extreme attenuations of $A_{V,\,\mathrm{stellar}} > 1$. Other parameters of our SED fits such as the stellar metallicity and $\log U$ remain consistent within the errors. Additionally, the gas-phase metallicities derived from optical emission line ratios remained consistent within the errors (Rowland et al. 2025). Thus, we conclude that our dust attenuation curves make minimal difference to the derived properties of the REBELS-IFU galaxies due to the moderate $A_{V,\,\mathrm{stellar}}$ values. Future spatially resolved analysis of these galaxies is needed to see whether other effects, such as outshining (e.g. Giménez-Arteaga et al. 2024), significantly affect physical properties obtained from the integrated spectra.

5.5 Intrinsic spectra

By correcting the fitted SED models with the dust attenuation curves, we obtained an intrinsic spectrum for each galaxy with the effect of dust removed. The intrinsic UV slope can reveal information about the recent SFH and metal enrichment history, as well as constraining the stellar IMF. The values measured for our sample shown in Fig. 6 range between $\beta_0 = -2.05$ and $\beta_0 = -2.33$. This is in good agreement with results using photometry from Bowler et al. (2024) for the REBELS galaxies, who found intrinsic slopes between $\beta_0 = -2.3$ and $\beta_0 = -2.5$. The intrinsic slopes also agree with the value of $\beta_0 = -2.30 \pm 0.15$ from SED fits to $2<z<3$ star-forming galaxies of similar masses by McLure et al. (2018). The intrinsic UV-slope values are all greater than the theoretical minimum value of $\beta_0 = -2.6$ obtained by assuming a young ($\lesssim$30 Myr), dust-free stellar population with maximum nebular continuum emission that reddens the UV slope (e.g. Cullen et al. 2017; Reddy et al. 2018). Thus, our results imply that the massive REBELS galaxies are more evolved with populations of less massive stars with redder intrinsic spectra already present, although some models find that these slopes can be produced more quickly with higher stellar metallicities (Topping et al. 2022b). The SED fits for the galaxies with the redder intrinsic UV slopes also tend to have higher metallicities. Higher metallicities cause redder UV slopes since the

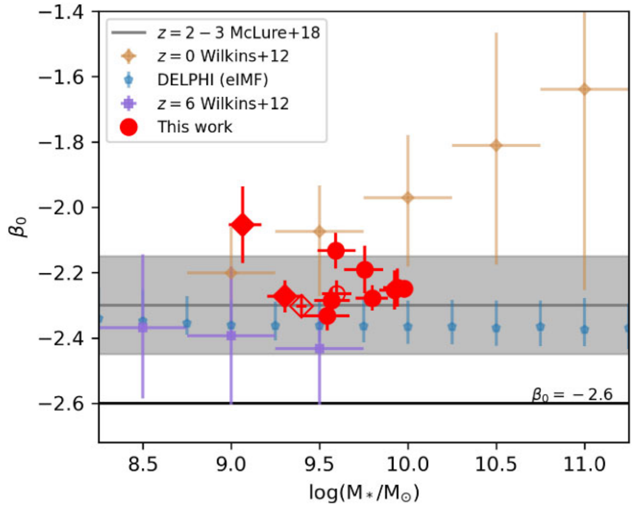

Figure 6. The intrinsic UV-continuum slopes, β_0, plotted against stellar mass, $M_\star$, are shown in red. These were obtained from applying the dust attenuation curves to the fitted SED model and have a mean value of $\beta_0 = -2.24 \pm 0.07$ implying that these galaxies contain evolved stellar populations. The horizontal black line shows the theoretical minimum value of $\beta_0 = -2.6$ (Cullen et al. 2017). The value of $\beta_0 = -2.3 \pm 0.15$ from SED fits of star-forming galaxies at $2<z<3$ from McLure et al. (2018) is shown in grey. The brown diamonds and purple squares show the modelling results from Wilkins et al. (2012) for galaxies at $z = 0$ and $z = 6$, respectively. The blue pentagons show the intrinsic slopes from DELPHI for a model whose IMF varies depending on redshift and metallicity (eIMF; Mauerhofer et al., in preparation).

stellar absorption features in the rest-UV increase with metallicity (e.g. Calzetti et al. 1994; Calabrò et al. 2021).

Simulations have suggested that redshift is the most important factor for setting β_0 at $z \geq 6$ since the correlations between β_0 and galaxy properties such as the SFR, intrinsic UV luminosity, and stellar mass flatten out with redshift (Wilkins et al. 2012). In Fig. 6, we see a weak negative correlation with mass such that the sources with higher masses have bluer intrinsic UV slopes. The $z = 6$ simulation results from Wilkins et al. (2012) also exhibit a slight downward trend with mass, which is the opposite trend to that seen at $z = 0$. Our intrinsic UV slopes also show rough consistency with more recent results from the semi-analytical galaxy formation code DELPHI (Mauerhofer et al., in preparation). We show the intrinsic UV slope from their eIMF model (but note that the values for their fiducial model are almost identical). This model has a variable IMF that depends on redshift and metallicity such that the IMF becomes more top-heavy at higher redshift and lower metallicities. This allows the model to reproduce a UV luminosity function consistent with observations over a broad range of redshifts.

The range of intrinsic UV slopes seen demonstrates the validity of concerns about assuming a fixed intrinsic UV slope and the scatter this introduces to relations that assume a fixed value for this parameter (e.g. IRX–β), especially given that from the selection of these galaxies we might expect the REBELS-IFU sample to have similar intrinsic properties. This shows the value of spectroscopic observations at these redshifts and reinforces the known limitations of deriving dust attenuation curves from relations such as $A_{V,\,\mathrm{stellar}}$–$M_\star$ or IRX–β. While these may capture the average properties for a population of galaxies, we recommend caution when applying corrections to individual sources.

6 CONCLUSIONS

We measure the dust attenuation curves of 12 massive ($9 < \log(M_\star/\mathrm{M}_\odot) < 10$) Lyman-break galaxies from *JWST* NIRSpec spectra at $z \simeq 6.5$–7.7. Our key findings are

(i) We find that the dust attenuation curves for individual galaxies exhibit a range of slopes. The slopes correlate with $A_{V,\,\mathrm{stellar}}$, but there is no clear dependence on stellar mass, M_{UV}, or gas-phase metallicity. Comparing this to empirical models suggests that the most important factor driving the steepness variation in the attenuation curves is dust-star geometry and not differences in the chemical composition or grain size distribution of the dust itself. This is supported by the clumpy geometry revealed by the spatial resolution of the IFU and the UV–FIR offsets seen in high-resolution ALMA observations of these sources.

(ii) The mean attenuation curve slope of $\delta = -0.19 \pm 0.15$ is consistent with the Calzetti-like ($\delta = 0$) relation in local starburst galaxies. The attenuation curves are generally flatter than local sources with no evidence for significant deviations in shape from local relations or very steep slopes of $\delta < -0.5$. We see $A_{V,\,\mathrm{stellar}}$ values indicative of moderate reddening ($A_{V,\,\mathrm{stellar}} = 0.1$–0.6 mag) that have a weak positive correlation with stellar mass, indicating that more massive galaxies are more dust-rich, as seen in local galaxies. This suggests that evolved galaxies at $z \simeq 7$ have similar dust properties to local sources.

(iii) Three dust attenuation curves (25 per cent of our sample) exhibit 2175 Å dust bumps with bump strengths at a significance of $\gtrsim 4\sigma$. These are the most massive galaxies at $z \simeq 7$ found to have this signature to date. This suggests that small carbonaceous dust grains may be present in a significant fraction of epoch of reionization galaxies. This places constraints on dust formation mechanisms since these grains must therefore form rapidly (Witstok et al. 2023b; Schneider & Maiolino 2024).

(iv) The differences in derived parameters such as stellar mass and metallicity using the flexible dust attenuation curve compared to assuming a Calzetti-like curve are negligible. The mass differences correlate with the attenuation curve slope, except for the galaxies with strong 2175 Å dust bumps. Not accounting for the deficit in the rest-UV flux caused by these dust bumps can cause the stellar masses to be overestimated by up to 0.4 dex.

(v) The derived intrinsic UV slopes from our fitting have a mean value of $\beta_0 = -2.24 \pm 0.07$ and are in good agreement with previous results from SED fits to photometry (Bowler et al. 2024). All are greater than the theoretical minimum value of $\beta_0 = -2.6$, suggesting that our galaxies contain evolved stellar populations. We recommend caution when using a fixed value for β_0 (e.g. when correcting SFRs from the IRX–β relation) given the range of values we obtain.

Gaining further insights into the dust properties of these sources will require utilizing the spatial resolution of the IFU and complementary ALMA observations available for these sources. For example, we can make spatially resolved measurements of the rest-frame UV slope and Balmer decrement allowing us to investigate the spatial distribution of dust, gas, and stars within these sources. These observations can also reveal to what extent effects such as outshining affect the properties measured from the integrated spectra. For six of the REBELS-IFU galaxies, high-resolution (up to 0.15 arcsec) ALMA Band 6 observations have recently been obtained (see Rowland et al. 2024, for REBELS-25 and Phillips et al., in preparation). This will allow us to investigate how rest-UV and rest-optical features correlate with the position of the dust continuum detections, further revealing the properties of dust in the first Gyr of the Universe.

ACKNOWLEDGEMENTS

The authors would like to thank the anonymous referee, whose comments helped to improve this manuscript. We thank the authors of Nagaraj et al. (2022) and Salim et al. (2018) for kindly sharing their data from these papers. We thank the authors of Markov et al. (in preparation) for allowing us to show a subsample of their upcoming results. RB acknowledges support from an STFC Ernest Rutherford Fellowship (grant number ST/T003596/1). MS acknowledges support from the European Research Commission Consolidator Grant 101088789 (SFEER), from the CIDEGENT/2021/059 grant by Generalitat Valenciana, and from project PID2023-149420NB-I00 funded by MICIU/AEI and by ERDF/EU. MA acknowledges support from ANID BASAL project FB210003 and ANID MILENIO NCN2024_112. PD acknowledges support from the NWO grant 016.VIDI.189.162 ('ODIN') and warmly thanks the European Commission's and University of Groningen's CO-FUND Rosalind Franklin program. AF acknowledges support from the ERC Advanced Grant INTERSTELLAR H2020/740120. JAH acknowledges support from the ERC Consolidator Grant 101088676 ('VOYAJ'). NSS gratefully acknowledges the support of the Research Foundation – Flanders (FWO Vlaanderen) grant 1290123N.

This work is based on observations made with the NASA/ESA/CSA *JWST*. The data were obtained from the Mikulski Archive for Space Telescopes at the Space Telescope Science Institute, which is operated by the Association of Universities for Research in Astronomy, Inc., under NASA contract NAS 5-03127 for *JWST*. These observations are associated with programs #1626 and #2659.

DATA AVAILABILITY

The data used in this manuscript will be made available to others upon reasonable request to the authors.

REFERENCES

Akins H. B. et al., 2022, ApJ, 934, 64
Algera H. S. B. et al., 2024a, MNRAS, 527, 6867
Algera H. et al., 2024b, preprint (arXiv:2408.02267)
Algera H. et al., 2025, preprint (arXiv:2501.10508)
Austin D. et al., 2024, preprint (arXiv:2404.10751)
Bakx T. J. L. C. et al., 2021, MNRAS, 508, L58
Barisic I. et al., 2017, ApJ, 845, 41
Barrufet L. et al., 2023, MNRAS, 522, 3926
Battisti A. J., Calzetti D., Chary R.-R., 2016, ApJ, 818, 13
Battisti A. J., Calzetti D., Chary R.-R., 2017, ApJ, 840, 109
Battisti A. J., da Cunha E., Shivaei I., Calzetti D., 2020, ApJ, 888, 108
Battisti A. J. et al., 2022, MNRAS, 513, 4431
Battisti A. J., Shivaei I., Park H. J., Decleir M., Calzetti D., Mathew J., Wisnioski E., da Cunha E., 2024, preprint (arXiv:2412.03690)
Bendo G. J. et al., 2023, MNRAS, 522, 2995
Béthermin M. et al., 2020, A&A, 643, A2
Boquien M. et al., 2022, A&A, 663 A50
Bouwens R. J. et al., 2009, ApJ, 705, 936
Bouwens R. J. et al., 2012, ApJ, 754, 83
Bouwens R. J. et al., 2014, ApJ, 793, 115
Bouwens R. J., Smit R., Labbé I., Franx M., Caruana J., Oesch P., Stefanon M., Rasappu N., 2016, ApJ, 831, 176
Bouwens R. J. et al., 2022, ApJ, 931, 160
Bowler R. A. A., Dunlop J. S., McLure R. J., McLeod D. J., 2017, MNRAS, 466, 3612
Bowler R. A. A., Bourne N., Dunlop J. S., McLure R. J., McLeod D. J., 2018, MNRAS, 481, 1631
Bowler R. A. A., Cullen F., McLure R. J., Dunlop J. S., Avison A., 2022, MNRAS, 510, 5088
Bowler R. A. A. et al., 2024, MNRAS, 527, 5808
Bruzual G., Charlot S., 2003, MNRAS, 344, 1000
Bruzual A. G., Magris G., Calvet N., 1988, ApJ, 333, 673
Calabrò A. et al., 2021, A&A, 646, A39
Calzetti D., 1997, in H. Waller William AIP Conf. Proc. Vol. 408, The Ultraviolet Universe at Low and High Redshift. Am. Inst. Phys., New York, p. 403
Calzetti D., Kinney A. L., Storchi-Bergmann T., 1994, ApJ, 429, 582
Calzetti D., Armus L., Bohlin R. C., Kinney A. L., Koornneef J., Storchi-Bergmann T., 2000, ApJ, 533, 682
Carnall A. C., McLure R. J., Dunlop J. S., Davé R., 2018, MNRAS, 480, 4379
Carnall A. C. et al., 2019, MNRAS, 490, 417
Castellano M. et al., 2014, A&A, 566, A19
Charlot S., Fall S. M., 2000, ApJ, 539, 718
Chevallard J., Charlot S., Wandelt B., Wild V., 2013, MNRAS, 432, 2061
Cochrane R. K., Anglés-Alcázar D., Cullen F., Hayward C. C., 2024, ApJ, 961, 37
Cooper O. R. et al., 2024, preprint (arXiv:2410.08387)
Cullen F., McLure R. J., Khochfar S., Dunlop J. S., Vecchia C. D., 2017, MNRAS, 470, 3006
Cullen F. et al., 2018, MNRAS, 476, 3218
Cullen F. et al., 2024, MNRAS, 531, 997
da Cunha E. et al., 2021, ApJ, 919, 30
De Looze I. et al., 2014, A&A, 568, A62
Decleir M. et al., 2019, MNRAS, 486, 743
Di Mascia F., Pallottini A., Sommovigo L., Decataldo D., 2024, preprint (arXiv:2407.01662)
Draine B., 2003, ARA&A, 41, 241
Duncan K. et al., 2014, MNRAS, 444, 2960
Dunlop J. S. et al., 2013, MNRAS, 432, 3520
Faisst A. L. et al., 2017, ApJ, 847, 21
Faisst A. L. et al., 2020, ApJS, 247, 61
Ferland G. J. et al., 2017, Rev. Mex. Astron. Astrofis., 53, 385
Ferrara A. et al., 2022, MNRAS, 512, 58
Fitzpatrick E. L., Massa D., 2007, ApJ, 663, 320
Fudamoto Y. et al., 2020, A&A, 643, A4
Fudamoto Y. et al., 2021, Nature, 597, 489
Giménez-Arteaga C. et al., 2024, A&A, 686, A63
Gordon K. D., Misselt K. A., Witt A. N., Clayton G. C., 2001, ApJ, 551, 269
Gordon K. D., Clayton G. C., Misselt K. A., Landolt A. U., Wolff M. J., 2003, ApJ, 594, 279
Gordon K. D. et al., 2024, ApJ, 970, 51
Guo Y. et al., 2015, ApJ, 800, 39
Harikane Y. et al., 2020, ApJ, 896, 93
Hashimoto T. et al., 2019, PASJ, 71 109
Heintz K. E. et al., 2025, A&A, 693, A60
Hirashita H., Murga M. S., 2020, MNRAS, 492, 3779
Huertas-Company M. et al., 2016, MNRAS, 462, 4495
Huertas-Company M. et al., 2024, A&A, 685, A48
Inami H. et al., 2022, MNRAS, 515, 3126
Inoue A. K., 2005, MNRAS, 359, 171
Inoue A. K., Buat V., Burgarella D., Panuzzo P., Takeuchi T. T., Iglesias-Paramo J., 2006, MNRAS, 370, 380
Kohandel M., Pallottini A., Ferrara A., Carniani S., Gallerani S., Vallini L., Zanella A., Behrens C., 2020, MNRAS, 499, 1250
Kriek M., Conroy C., 2013, ApJ, 775, L16
Kroupa P., 2001, MNRAS, 322, 231
Langeroodi D., Hjorth J., Ferrara A., Gall C., 2024, preprint (arXiv:2410.14671)
Le Fèvre O. et al., 2020, A&A, 643, A1

Leja J., Johnson B. D., Conroy C., van Dokkum P. G., Byler N., 2017, ApJ, 837, 170
Leja J., Carnall A. C., Johnson B. D., Conroy C., Speagle J. S., 2019, ApJ, 876, 3
Li A., Liang S. L., Kann D. A., Wei D. M., Klose S., Wang Y. J., 2008, ApJ, 685, 1046
Liddle A. R., 2007, MNRAS, 377, L74
Lin Y. H., Hirashita H., Camps P., Baes M., 2021, MNRAS, 507, 2755
Lines N. E. P. et al., 2024, preprint (arXiv:2409.10963)
Lower S., Narayanan D., Leja J., Johnson B. D., Conroy C., Davé R., 2020, ApJ, 904, 33
Lower S., Narayanan D., Leja J., Johnson B. D., Conroy C., Davé R., 2022, ApJ, 931, 14
McLure R. J. et al., 2018, MNRAS, 476, 3991
Markov V., Gallerani S., Pallottini A., Sommovigo L., Carniani S., Ferrara A., Parlanti E., Mascia F. D., 2023, A&A, 679, A12
Markov V., Gallerani S., Ferrara A., Pallottini A., Parlanti E., Mascia F. D., Sommovigo L., Kohandel M., 2024, ApJ, 217, 425
Marrone D. P. et al., 2018, Nature, 553, 51
Massa D., Gordon K. D., Fitzpatrick E. L., 2022, ApJ, 925, 19
Meurer G. R., Heckman T. M., Calzetti D., 1999, ApJ, 521, 64
Mitsuhashi I. et al., 2024, ApJ, 971, 161
Morales A. M. et al., 2024, ApJ, 964, L24
Nagaraj G., Forbes J. C., Leja J., Foreman-Mackey D., Hayward C. C., 2022, ApJ, 932, 54
Narayanan D., Conroy C., Davé R., Johnson B. D., Popping G., 2018, ApJ, 869, 70
Noll S. et al., 2009, A&A, 499, 69
Pallottini A. et al., 2022, MNRAS 513 4 5621–5641
Planck Collaboration VI, 2020, A&A, 641, A6
Reddy N. A., Erb D. K., Pettini M., Steidel C. C., Shapley A. E., 2010, ApJ, 712, 1070
Reddy N. A. et al., 2015, ApJ, 806, 259
Reddy N. A. et al., 2018, ApJ, 869, 92
Reddy N. A. et al., 2020, ApJ, 902, 123
Rezaee S., Reddy N., Shivaei I., Fetherolf T., Emami N., Khostovan A. A., 2021, MNRAS, 506, 3588
Roberts-Borsani G. et al., 2024, ApJ, 976, 193
Rowland L. E. et al., 2024, MNRAS, 535, 2068
Rowland L. E. et al., 2025, preprint (arXiv:2501.10559)
Salim S., Narayanan D., 2020, ARA&A, 58, 529
Salim S. et al., 2016, ApJS, 227, 2
Salim S., Boquien M., Lee J. C., 2018, ApJ, 859, 11
Sanders R. L. et al., 2024a, preprint (arXiv:2408.05273)
Sanders R. L., Shapley A. E., Topping M. W., Reddy N. A., Brammer G. B., 2024b, ApJ, 962, 24
Schneider R., Maiolino R., 2024, A&AR, 32, 2
Schouws S. et al., 2023, ApJ, 954, 103
Schwarz G., 1978, Ann. Stat., 6
Seon K.-I., Draine B. T., 2016, ApJ, 833, 201
Shivaei I. et al., 2020a, ApJ, 899, 117
Shivaei I., Darvish B., Sattari Z., Chartab N., Mobasher B., Scoville N., Rieke G., 2020b, ApJ, 903, L28
Shivaei I. et al., 2022, MNRAS, 514, 1886
Sommovigo L. et al., 2022, MNRAS, 513, 3122
Sommovigo L. et al., 2025, preprint (arXiv:2502.13240)
Stanway E. R., Eldridge J. J., 2018, MNRAS, 479, 75
Tacchella S. et al., 2022, ApJ, 927, 170
Tamura Y. et al., 2019, ApJ, 874, 27
Topping M. W. et al., 2022a, MNRAS, 516, 975
Topping M. W., Stark D. P., Endsley R., Plat A., Whitler L., Chen Z., Charlot S., 2022b, ApJ, 941, 153
Topping M. W. et al., 2024, MNRAS, 529, 4087
Tripodi R. et al., 2024, A&A, 692, A184
Watson D., Christensen L., Knudsen K. K., Richard J., Gallazzi A., Michałowski M. J., 2015, ApJ, 803, 1
Whitler L., Stark D. P., Endsley R., Leja J., Charlot S., Chevallard J., 2023, MNRAS, 519, 5859
Wilkins S. M., Bunker A. J., Stanway E., Lorenzoni S., Caruana J., 2011, MNRAS, 417, 717
Wilkins S. M., Gonzalez-Perez V., Lacey C. G., Baugh C. M., 2012, MNRAS, 424, 1522
Witstok J. et al., 2022, MNRAS, 515, 1751
Witstok J., Jones G. C., Maiolino R., Smit R., Schneider R., 2023a, MNRAS, 523, 3119
Witstok J. et al., 2023b, Nature, 621, 267
Witt A. N., Gordon K. D., 2000, ApJ, 528, 799
Witt A. N., Thronson H. A.,, Jr, Capuano J. M.,, Jr, 1992, ApJ, 393, 611
Yamanaka S., Yamada T., 2019, PASJ, 71 51

APPENDIX A: SED MODEL TESTS

This section describes the tests we performed to check that our SED fitting procedure accurately recovers the slope of the dust attenuation curve. We used BAGPIPES to generate model galaxy SEDs with the same observed wavelength coverage as the real NIRSpec spectra for our sample. For each of the 12 REBELS-IFU galaxies, we take the best-fitting parameters from our SED fits to the real spectra for all the properties except for $A_{V,\,\mathrm{stellar}}$ and δ. We then generate eight model galaxy spectra for four values of $\delta = [0.0, -0.2, -0.4, -0.6]$ and two values of $A_{V,\,\mathrm{stellar}} = [0.2, 0.5]$. These are representative of the range of values that we see in our sample. We then add realistic Gaussian noise to the model SED. To do this, we fit a second-order polynomial to the error on the observed spectrum of one of our observations to capture the shape of its wavelength dependence and then scale this according to the median rest-UV flux between rest-frame wavelengths of 1216 and 3500 Å. This produces spectra with noise levels that are visually similar to what we see in the real spectra. We then use the same fitting procedure described in Section 3.

In Fig. A1, we fit contours to the recovered dust attenuation curve slope against the slope inputted into the model. The peak of each distribution at each δ value is close to the 1-to-1 line, confirming that we can accurately recover the attenuation curve. Given that some of these $A_{V,\,\mathrm{stellar}}$–δ scenarios may be physically unlikely, the true recoverability is expected to be better than implied here. By plotting the contours at the same levels in both plots, we can see that the scatter in recovered slopes is lower at higher $A_{V,\,\mathrm{stellar}}$, as we would expect since at lower $A_{V,\,\mathrm{stellar}}$ the dust will have a smaller impact on the observed spectrum. This is reflected in the larger error bars on δ values for sources with low $A_{V,\,\mathrm{stellar}}$ in Fig. 3. The slope is also better recovered in both $A_{V,\,\mathrm{stellar}}$ cases when it is steeper, confirming that if steep slopes were present in our sample we would recover them.

In Fig. A2, we show the impact of assuming different SFHs on our results. We run the BAGPIPES fits to the observed spectra with continuity, constant, double power-law, exponential, delayed, and lognormal SFHs. The largest deviations from the fiducial NP results we present in the rest of this work, $\delta_{\mathrm{NP,BC03}}$, are seen when using the constant SFH, which recovers very flat slopes. This is unsurprising given it is the model with the least flexibility. However, in all cases, we recover the same trends as those shown in Figs 3 and 4. Thus, we can be confident that our results and conclusions are not significantly affected by our choice of SFH. We also run using the NP SFH but with the BPASS stellar population models and find that the recovered slopes are consistent within the errors.

To test the sensitivity of our SED fitting results to the optical emission lines in our spectra, we mask the wavelengths with strong emission lines ([O II] λ3727 to H γ, H β to [O III] λ5007, and greater than H α) and run BAGPIPES fits with the same fitting procedure as described in Section 3. In the left panels of Fig. A3, we show the

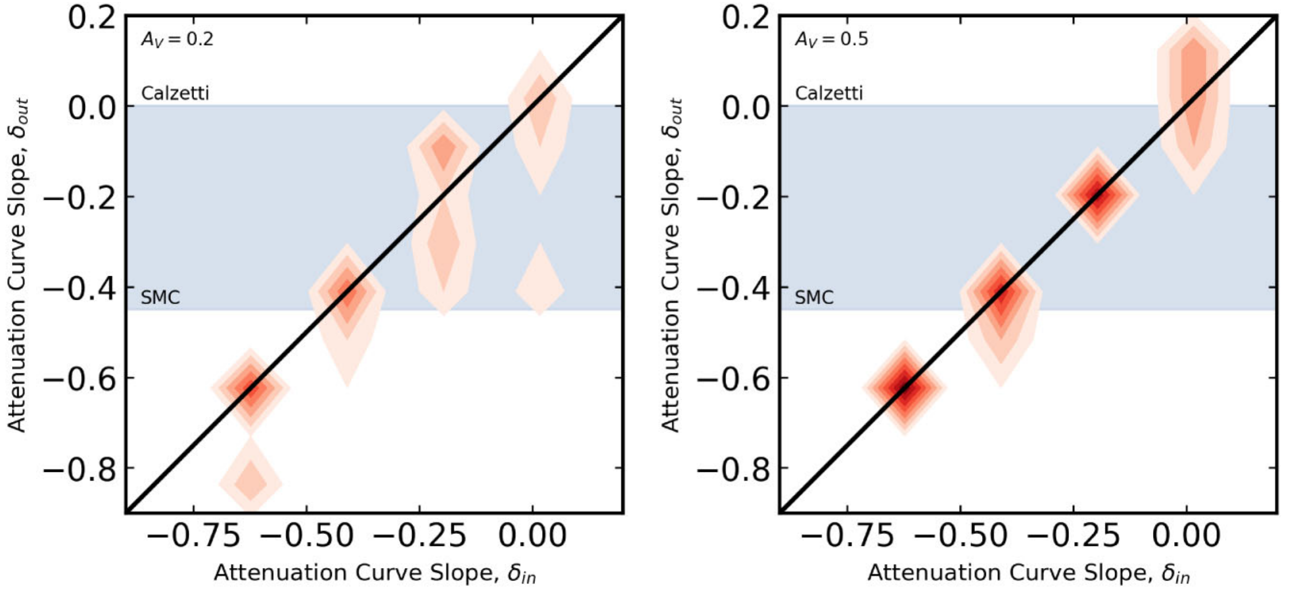

Figure A1. Contour plot for the fitted dust attenuation curve slope, $\delta_{\rm out}$, plotted against the slope of the input model $\delta_{\rm in}$. For each of our 12 galaxies, we generate 8 model galaxy spectra for 4 values of $\delta = [0.0, -0.2, -0.4, -0.6]$ and two values of $A_{V,\,\rm stellar} = [0.2, 0.5]$. We see that the dust attenuation curve slope is recovered well, particularly when the curve is steeper. As expected, the scatter is also lower at higher $A_{V,\,\rm stellar}$ since dust has a greater effect on the spectra.

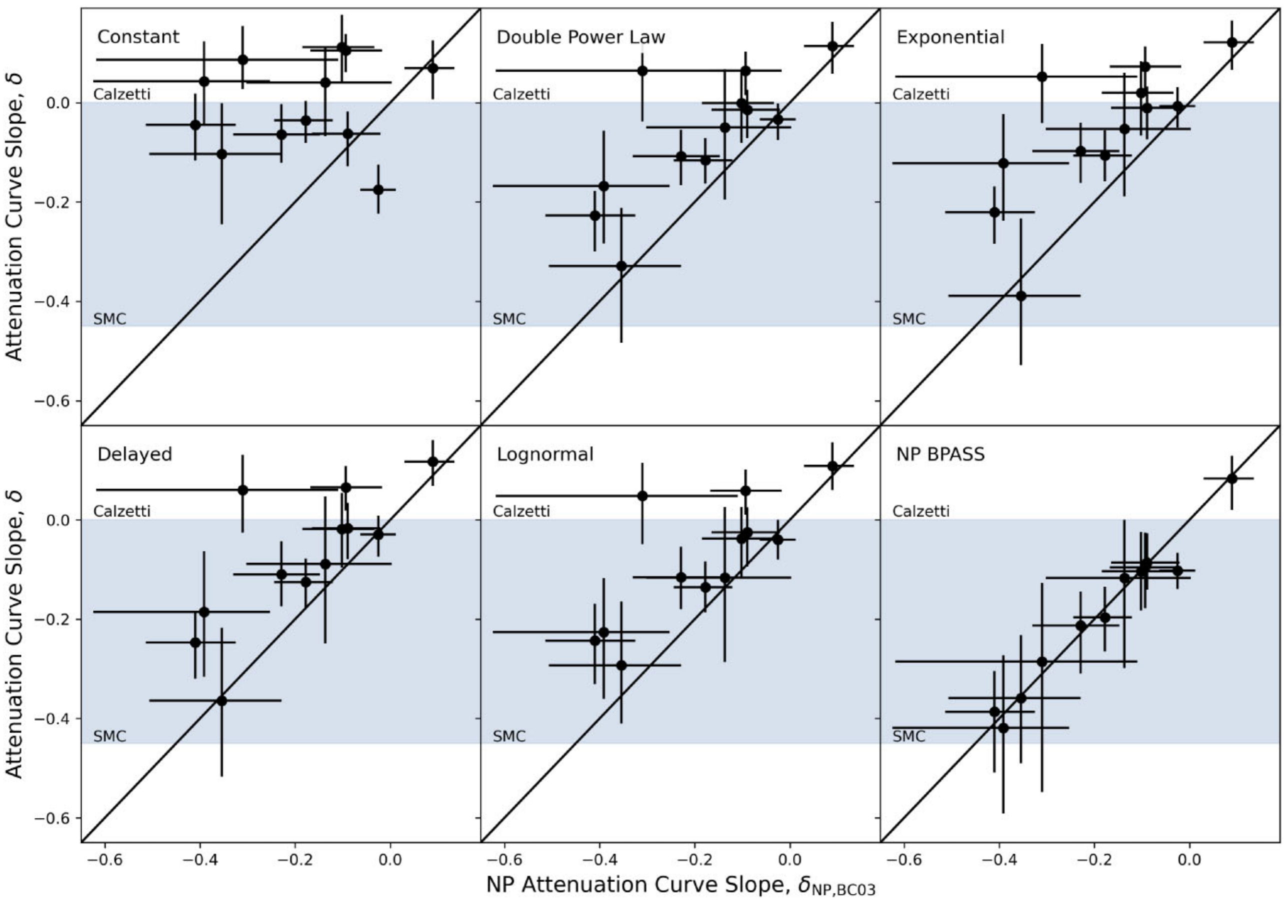

Figure A2. The fitted dust attenuation curve slope, δ, for different SFHs compared to the values used throughout the rest of this work that used an NP SFH. We also show the slopes recovered when using the NP SFH with the BPASS stellar population models are consistent within the errors with our fiducial fits.

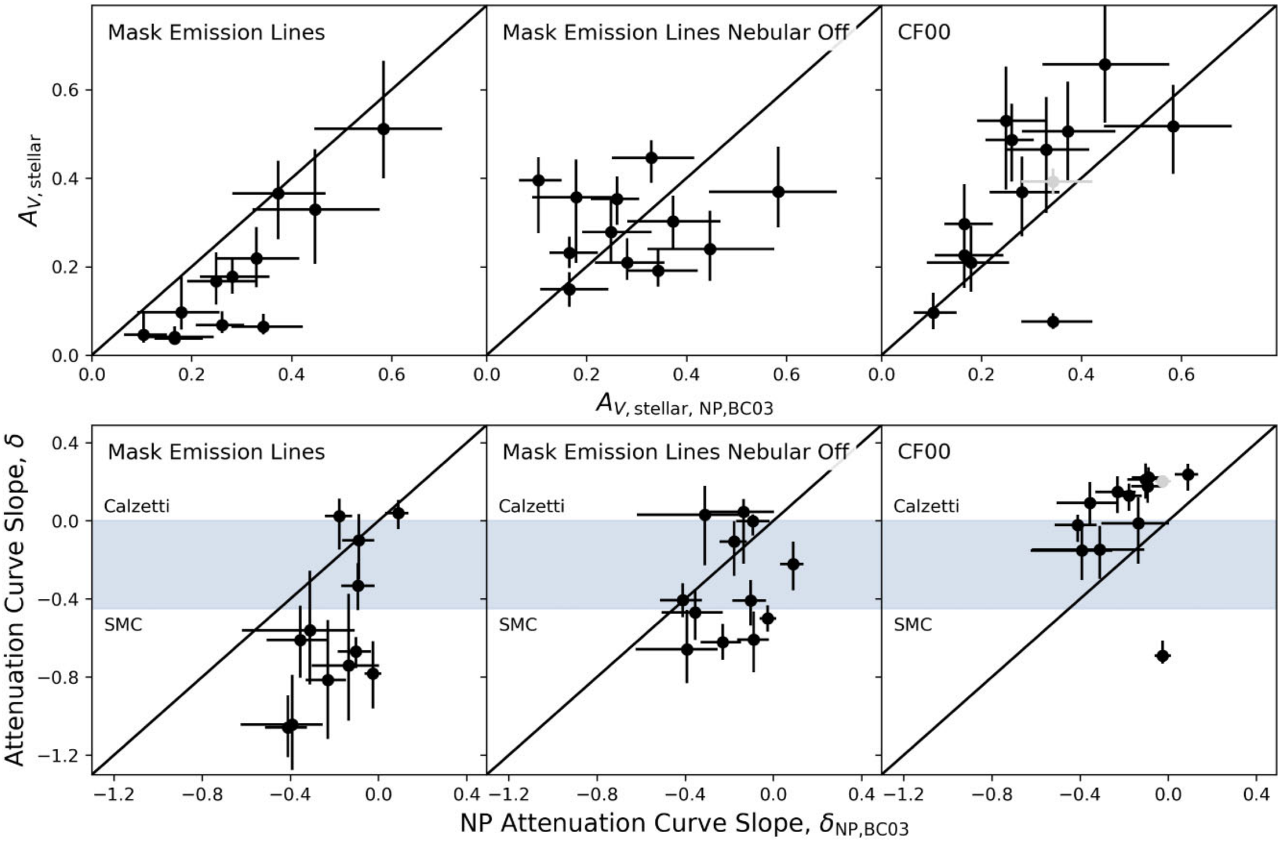

Figure A3. The fitted stellar continuum V-band attenuation magnitude $A_{V,\mathrm{stellar}}$, and attenuation curve slope, δ, for SED fit tests compared to the values used throughout the rest of this work that used an NP SFH and Salim et al. (2018) dust attenuation curve parametrization. With the emission lines in the observed spectra masked (left), we obtain systematically lower $A_{V,\mathrm{stellar}}$ values and steeper attenuation curves. When the emission lines in the spectra are masked and the nebular component of the SED is switched off (middle), the attenuation curve slopes are more consistent. On the right, we show the results when using the Charlot & Fall (2000) dust attenuation curve parametrization. The Charlot & Fall (2000) model systematically recovers shallower slopes and higher $A_{V,\mathrm{stellar}}$ values. The exception is REBELS-15, although we show in grey that when masking the wavelength region around the dust bump we obtain a shallower slope.

recovered $A_{V,\mathrm{stellar}}$ and δ values. While the recovered values show a strong positive correlation with those obtained when fitting with the emission lines, the $A_{V,\mathrm{stellar}}$ values are systematically lower and the fitted attenuation curves tend to be steeper. We note from the corner plots that the parameters such as η and $\log U$, which we would expect to rely most on these emission lines, become very poorly constrained. The SFR in the most recent SFH bin was also higher in these fits compared to the fiducial (i.e. effectively younger ages), which can be linked to the steeper attenuation curves. In the middle panel of Fig. A3, we show the results of SED fitting with the emission lines masked and the nebular emission component switched off. Here, we see closer agreement between the attenuation curve slopes, although some fitted curves are still steeper. This could be explained by the fact that masking the major emission lines does not remove all of the contribution to the flux from the nebular emission. This will make the longer wavelengths appear less attenuated and thus the fitted attenuation curve is steeper. These tests suggest that the emission lines do play some role in breaking the degeneracies in the SED fitting, such as between the dust attenuation and metallicity. We caveat again that these results assume that the slope of the attenuation curve affecting the nebular emission is the same as that affecting the stellar continuum.

In the right panel of Fig. A3, we compare the $A_{V,\mathrm{stellar}}$ and δ values recovered when SED fitting with the Charlot & Fall (2000) dust attenuation curve parametrization. We note that this model is reasonably sensitive to the prior on $n = -\delta + n_{\mathrm{Calzetti}} = -\delta + 0.75$, for which we adopt a Gaussian prior with mean $n_{\mu} = 1$ and standard deviation $n_{\sigma} = 0.2$, similar to Carnall et al. (2019). We also note that the BAGPIPES implementation of this model does not include a dust bump term. This model tends to fit slightly larger $A_{V,\mathrm{stellar}}$ values and flatter attenuation curves in all but one case. A steep slope is recovered for REBELS-15, but a shallower slope is recovered if the wavelength range around the dust bump is masked (shown in grey). Apart from these systematic shifts, the other trends presented in this work are unchanged if we adopt this dust attenuation curve shape parametrization. The cause of these systematic shifts is the difference in shape, with the Charlot & Fall (2000) attenuation curve falling below the Salim et al. (2018) parametrization for the majority of the wavelength range we fit over for the same value of δ. Given the systematic shift in both $A_{V,\mathrm{stellar}}$ and δ, the overall attenuation magnitudes at a given wavelength, A_{λ}, are reasonably consistent between the two parametrizations. We opt to present the results using the Salim et al. (2018) parametrization since this allows us to include a dust bump term in the attenuation curve, it uses the Calzetti et al. (2000) attenuation curve that is based on observations of local starburst galaxies, and is less sensitive to the priors placed on the attenuation curve slope.

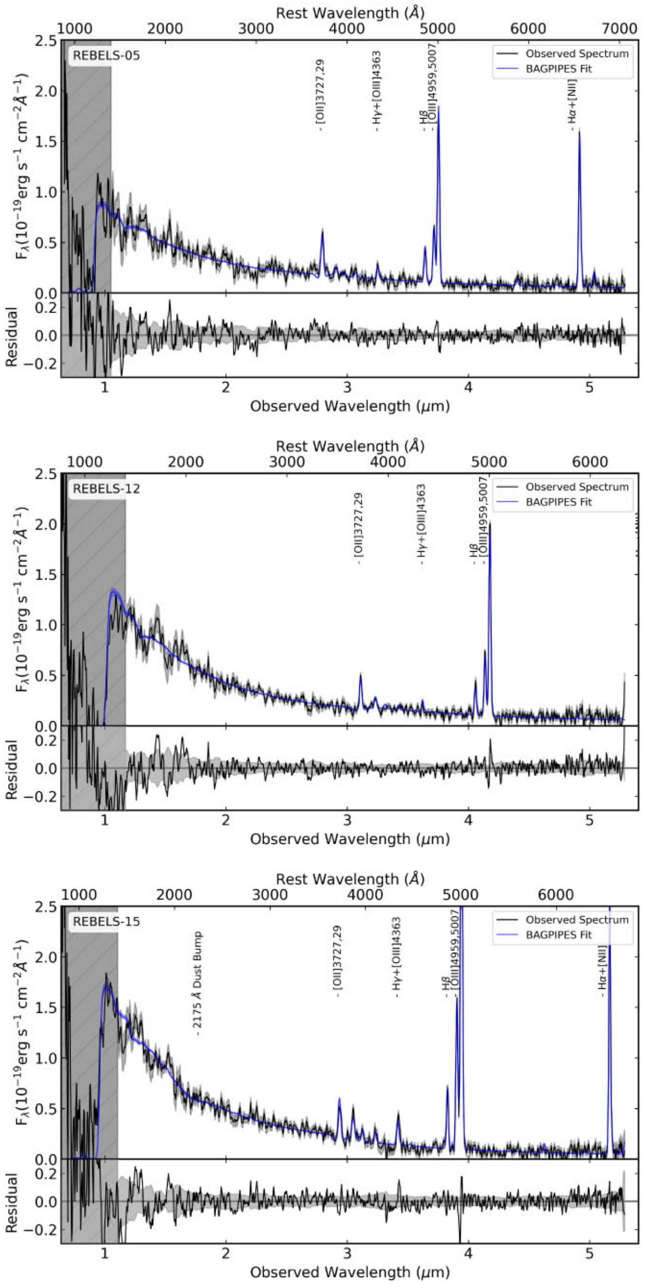

Figure B1. Full NIRSpec PRISM spectra for the REBELS-IFU galaxies with the 1σ error shown by the grey-shaded region. The best-fitting SED model using a flexible dust attenuation curve is shown in blue. The spectrum is masked below a rest-frame wavelength of 1400 Å to exclude effects caused by potential Ly α damping and instrumental effects at low wavelengths. The bottom panel in each plot shows the fit residuals. REBELS-08, REBELS-15, and REBELS-25 show evidence for a 2175 Å dust bump.

APPENDIX B: SED FITS TO THE SPECTRA FOR ALL 12 GALAXIES

In Figs B1 and B2, we show the full NIRSpec PRISM spectrum for each of the 12 REBELS galaxies in our sample and the best-fitting SED model. These fits were performed using BAGPIPES with a flexible dust attenuation curve, as described in Section 3.

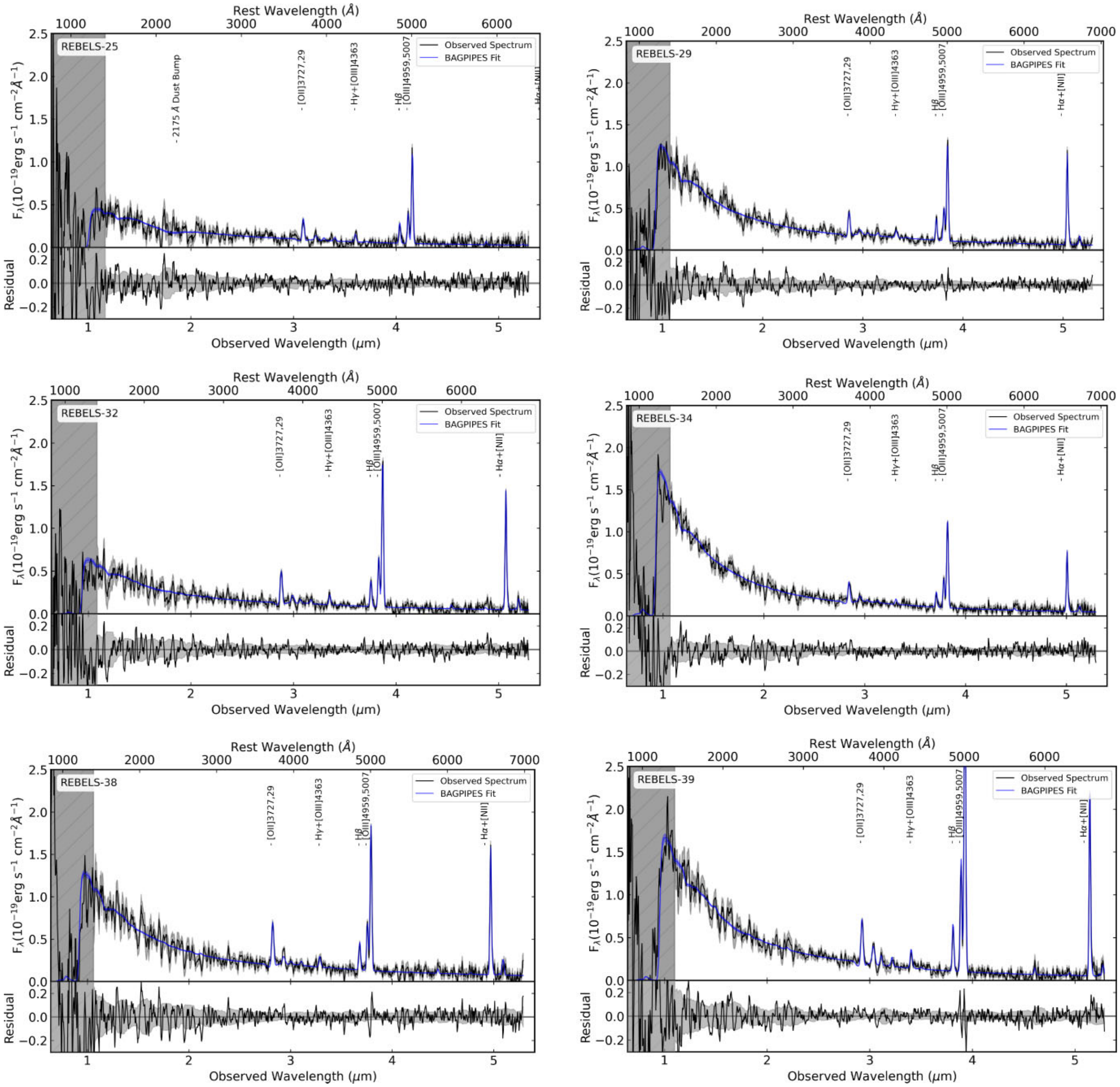

Figure B2. Full NIRSpec PRISM spectra for the REBELS-IFU galaxies with the 1σ error shown by the grey-shaded region. The best-fitting SED model using a flexible dust attenuation curve is shown in blue. The spectrum is masked below a rest-frame wavelength of 1400 Å to exclude effects caused by potential Ly α damping and instrumental effects at low wavelengths. The bottom panel in each plot shows the fit residuals. REBELS-08, REBELS-15, and REBELS-25 show evidence for a 2175 Å dust bump.

This paper has been typeset from a TEX/LATEX file prepared by the author.